

Accepted Manuscript

Coupling rigid bodies motion with single phase and two-phase compressible flows on unstructured meshes

Quentin Carmouze, François Fraysse, Richard Saurel, Boniface Nkonga

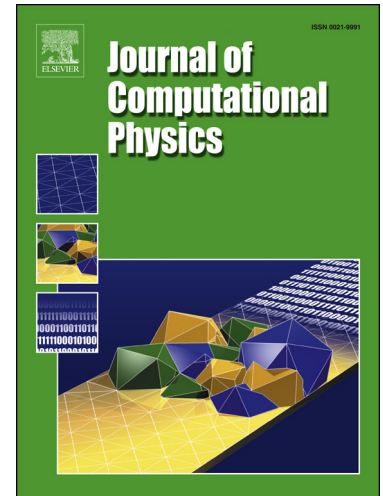
PII: S0021-9991(18)30546-1
DOI: <https://doi.org/10.1016/j.jcp.2018.08.023>
Reference: YJCPH 8209

To appear in: *Journal of Computational Physics*

Received date: 5 April 2018
Revised date: 13 July 2018
Accepted date: 13 August 2018

Please cite this article in press as: Q. Carmouze et al., Coupling rigid bodies motion with single phase and two-phase compressible flows on unstructured meshes, *J. Comput. Phys.* (2018), <https://doi.org/10.1016/j.jcp.2018.08.023>

This is a PDF file of an unedited manuscript that has been accepted for publication. As a service to our customers we are providing this early version of the manuscript. The manuscript will undergo copyediting, typesetting, and review of the resulting proof before it is published in its final form. Please note that during the production process errors may be discovered which could affect the content, and all legal disclaimers that apply to the journal pertain.



Highlights

- A simple and efficient method is developed for rigid solids / fluid coupling on unstructured meshes.
- The method addresses solid rigid body motion on fixed meshes, simpler than those based on moving meshes.
- The present approach, a variant of Ghost-Cell methods, doesn't seem more accurate than existing ones but seems conceptually simpler and easier to implement.

Coupling rigid bodies motion with single phase and two-phase compressible flows on unstructured meshes

Quentin Carmouze^(1,2,3), François Fraysse⁽²⁾, Richard Saurel^(1,2) and Boniface Nkonga⁽³⁾

⁽¹⁾ Aix Marseille Univ, Centrale Marseille, LMA CNRS UMR 7031, Marseille, France

⁽²⁾ RS2N, Chemin de Gaumin, Saint-Zacharie 83640, France

⁽³⁾ University of Nice, LJAD UMR CNRS 7351, Parc Valrose, 06108 Nice Cedex, France

Abstract

A simple method is developed to couple accurately translational motion of rigid bodies to compressible fluid flows. Solid rigid bodies are tracked through a Level-Set function. Numerical diffusion is controlled thanks to a compressive limiter (Overbee) in the frame of MUSCL-type-scheme, giving an excellent compromise between accuracy and efficiency on unstructured meshes (Chiapolino et al., 2017). The method requires low resolution to preserve solid bodies' volume. Several coupling methods are then addressed to couple rigid body motion to fluid flow dynamics: a method based on stiff relaxation and two methods based on Ghost cells (Fedkiw et al., 1999) and immersed boundaries. Their accuracy and convergence rates are compared against an immersed piston problem in 1D having exact solution. The second Ghost cell method is shown to be the most efficient. It is then extended to multidimensional computations on unstructured meshes and its accuracy is checked against flow computations around cylindrical bodies. Reference results are obtained when the flow evolves around a rigid body at rest. The same rigid body is then considered with prescribed velocity moving in a flow at rest. Computed results involving wave dynamics match very well. The method is then extended to two-way coupling and illustrated to several examples involving shock wave interaction with solid particles as well as phase transition induced by projectiles motion in liquid-gas mixtures.

e-mails:

Quentin.carmouze@rs2n.eu

Francois.fraysse@rs2n.eu

Richard.saurel@univ-amu.fr

Boniface.nkonga@unice.fr

1 – Introduction

In fluid mechanics two approaches are used to address the relative motion between a rigid body and a fluid. The first one is also the most commonly used and consists in considering a fluid moving around a body at rest. Setting appropriate boundary conditions at inflows, outflows and walls this method gives

reliable results. A fundamental difficulty emerges rapidly as soon as two (or more) rigid bodies are present. For instance, a moving body in the presence of a distant wall at rest is problematic.

In the present approach rigid bodies are tracked on a fixed mesh with the help of Level-Set-type functions (Osher and Fedkiw, 2001). This function enables detection of fluids, solids and mixed cells. There are several advantages:

- The method allows solid body motion on fixed meshes and thus eliminates issues related to Lagrangian and ALE methods (Baum et al., 1994, Nkonga and Guillard, 1994, Nkonga, 2000);
- Surfaces are defined implicitly rather than explicitly as in the frame of Front Tracking (Glimm et al., 1998) and Interface Reconstruction methods (Youngs, 1984).

There are obviously drawbacks such as:

- Numerical smearing of the interface contour, that may result in solid body disappearance if the Level-Set function is resolved with insufficient accuracy ;
- Interface roughness effects due to mixed cells.

These issues become pregnant when dealing with unstructured grids as it is more difficult to control artificial smearing and roughness.

To be more precise regarding the state of the art of existing methods, it is worth to mention that accurate results can be obtained with ALE codes as well as cut-cells algorithms. In the frame of ALE methods it is possible to manage mesh deformation in the fluid with linear elasticity equations (Farhat et al., 2001, Barral and Alauzet, 2018). Several subtle operations are necessary to maintain a mesh of high quality. This is done to the price of code complexity and computational cost, but the interface between solid and fluid stays well defined, allowing accurate computation of boundary layers effects. The same remarks hold for cut-cells methods (Muralidharan, B. and Menon, 2018) where the mesh is not distorted, but needs special care with vanishing and emerging cells, as well as AMR (Berger and Colella, 1989) to reduce mesh roughness effects.

With the present alternative, already investigated by Liu et al. (2003), Wang et al. (2006), Liu et al. (2006), Liu et al. (2008), Zeng and Farhat (2012) to cite a few, the quest for simplicity dictates efforts. With the present contribution numerical smearing effects are reduced thanks to a specific limiter, straightforward to implement. Interface roughness effects are reduced with the help of appropriate velocity extrapolation from the fluid to the solid. AMR or mesh refinement of unstructured grids (Shewchuk, 2002) can be used to reach the required level of accuracy but are not addressed in the present work.

Recently a compressive limiter was introduced to sharpen diffuse interfaces in compressible two-phase flow modelling in the frame of ‘diffuse interfaces’ (Chiapolino et al., 2017, Saurel and Pantano, 2018). This limiter showed enhanced capturing properties with 2-3 cells only in the interfacial zone, when used in the frame of MUSCL-type-schemes and unstructured meshes. It is thus considered in the present contribution to solve the Level-Set function to control numerical smearing. Its ability to preserve volume and maintain shapes is examined and is shown to be reasonably accurate. In the present frame, translational motion only is considered, excluding rotational one.

The coupling between solid body motion and compressible fluid flow is then examined. It is first examined in one-way, with prescribed solid velocity and action on the surrounding fluid. Three methods of coupling are examined:

- The first one is also the simplest and considers stiff velocity relaxation between the fluid and solid.
- The second one considers Ghost cells in the solid where specific fluid state is prescribed in a given band of cells closed to the interface.
- The third one consists in an improvement of the former to improve its convergence. The Ghost state is modified to improve the surface pressure computation, improving shock and rarefaction waves formation in the fluid during impulsive motion.

Comparison of the various coupling methods is done in 1D with the help of an exact solution of an immersed piston set to impulsive motion, quite similar to the exact shock tube solution.

The coupling method is then extended to multi-D, posing extra difficulties as sliding effects between solid and fluid have to be considered in a context where the interface is arbitrarily rough, as a consequence of unstructured mesh.

The coupling method when the solid is moving in a fluid at rest is validated by comparing computational results when the solid is at rest and the fluid is moving through appropriate boundary conditions, as done in most CFD computation. It is then extended to two-way coupling, through the computation of pressure force integral over the solid surface. It enables update of the solid body velocity which in turn affects the fluid flow. Computational examples of shock – solid particles interaction are shown to illustrate method's capability.

In the area of solid-fluid coupling with Level-Set type methods, many contributions have to be mentioned such as for example, Liu et al. (2003), Wang et al. (2006), Liu et al. (2006), Liu et al. (2008), Zeng and Farhat (2012) this list being certainly not exhaustive. However it seems that important differences appear with the present contribution. First, Cartesian grids are considered instead of unstructured ones. Second, exact or approximate local Riemann problem solution is set in mixture cells to enforce interface conditions. In the present contribution, such ingredient is not used, this detail being important when dealing with sophisticated flow models, such as multiphase flow ones. Last, Ghost Cells in multi-D computations are filled with fluid state normal to the interface in a band (or layer) of cells of finite size. Determination of these cells in the normal direction to the interface may be challenging when dealing with unstructured grids. In the present contribution this issue is replaced by a simple averaging method.

Fluid-fluid and solid-fluid coupling with Level-Set methods have been addressed in the frame of unstructured meshes by Farhat et al. (2008, 2012), Wang et al. (2011) and possibly other authors. It seems that similar restrictions as the former lists with Cartesian grid approaches are present:

- Use of local Riemann problem solution,
- Sophisticated method for setting fluid state in the Ghost-Cell band.

The present approach doesn't seem more accurate than existing ones but seems conceptually simpler and easier to implement.

The paper is organized as follows. The Level-Set method and its numerical resolution are summarized in Section 2. Then, coupling methods are examined in Section 3. The compressible flow model is presented in this section and a reference solution is built to address an immersed piston set to motion impulsively. Three different coupling methods are detailed and tested against the exact solution of the immersed piston test. The method that matches best the results is then extended to multi-dimensions in Section 4. This section ends by validations of the coupling method in 2D with a supersonic flow. Section 5 extends to coupling method to two-way coupling through pressure force computation over each rigid body surface. Conclusions are given in Section 6.

2 – Motion of rigid bodies

Rigid bodies are tracked through the Level-Set function denoted by Φ , that is in the present approach aimed to model a Heaviside function. Let us consider a domain Ω having a subdomain Ω_f occupied by the fluid and another sub-domain Ω_s occupied by the solid body, as schematized in Fig. 2.1.

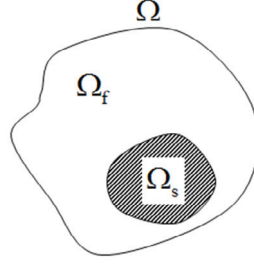


Figure 2.1 - Schematic representation of the solid and fluid sub-domains

The Level-Set function Φ indicates the presence of materials and interface at a given point of space \mathbf{M} . It is defined as,

$$\begin{cases} 1 \geq \Phi > 0 & \text{if } \mathbf{M} \in \Omega_s \\ 0 & \text{if } \mathbf{M} \in \Omega_f \cap \Omega_s \\ 0 > \Phi \geq -1 & \text{if } \mathbf{M} \in \Omega_f \end{cases} \quad (2.1)$$

With these definitions the zero level pays particular attention as it represents the solid-fluid interface. The Level-Set function obeys the transport equation,

$$\frac{\partial \Phi}{\partial t} + \bar{\mathbf{u}}_s \cdot \bar{\nabla} \Phi = 0 \quad (2.2)$$

where $\bar{\mathbf{u}}_s$ denotes the solid body velocity. As it is constant in the rigid body and only time dependent, Eq. (2.2) can be expressed in conservation form:

$$\frac{\partial \Phi}{\partial t} + \bar{\nabla} \cdot (\Phi \bar{\mathbf{u}}_s) = 0 \quad (2.3)$$

Note that considering uniform rigid body velocity excludes rotational motion. The main difficulty with the Level-Set method is to preserve body volume and shape. As a Heaviside function is initially set as $\Phi = 1$ in the solid and $\Phi = -1$ in the fluid, numerical smearing of the discontinuity may result rapidly in solid volume loss. As soon as two interfaces are present and mesh not enough refined solid body may disappear as time evolves. A typical example is shown in Fig. 2.4 when the MUSCL-Superbee method is used. Several methods are available to balance this weakness:

- When the Level-Set function is used as a distance function (different of definition in Eq. (2.1)), a re-initialization procedure is able to restore the correct function profile (Osher and Fedkiw, 2001).
- When it is aimed to model a Heaviside function, as in the present work, the interface can be sharpened with the help of artificial compressibility terms (Olsson et al., 2007, Shukla et al., 2010).

However these procedures require efforts, in particular in unstructured meshes and are consuming in computer resources.

For the sake of simplicity we adopt the method developed in Chiapolino et al. (2017) in the frame of diffuse interface modelling. This method was precisely designed to lower the numerical diffusion of so called 'diffuse interfaces' through a specific limiter, used to sharpen volume fraction profiles. This limiter (Overbee) is used in MUSCL-type-schemes (Van Leer, 1979) that are quite simple to implement in unstructured codes. Details of the implementation used in the present work are given in Chiapolino et al. (2017). The Overbee limiter is illustrated in Fig. 2.2 and corresponds to the upper bound of the first-order TVD region.

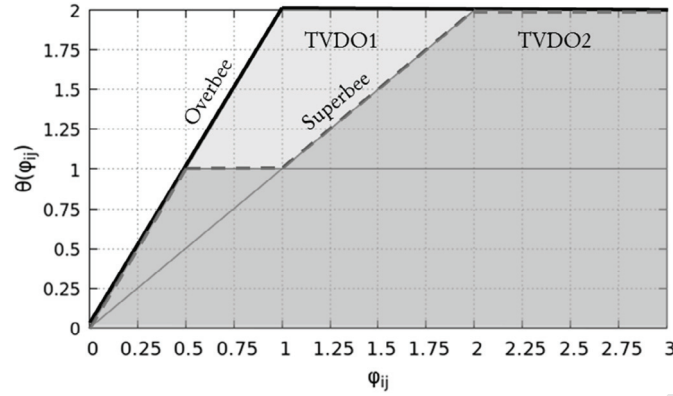


Figure 2.2- First-order and second-order TVD regions. The upper bounds of these regions correspond respectively to the Overbee and Superbee limiters.

The Overbee limiter used in the computational examples of the present paper reads:

$$\theta(\phi_{ij}) = \max \left[0, \min \left[2\phi_{ij}, 2 \right] \right], \quad (2.4)$$

where ϕ_{ij} represents the ratio of slopes between cells i and j .

This limiter was originally designed for volume fraction transport, where boundedness of this variable between 0 and 1 is mandatory, and used without modification with the Level-Set function. Thus, the signed property of this function is not used at the discrete level but used only to detect materials through Eq. (2.1). Efficiency of this limiter is illustrated in Fig. 2.3 where a comparison with Superbee is shown for the transport of a Heaviside function at prescribed velocity. Superbee was considered as the optimum bound for the design of limiters (Sweby, 1984). However, when dealing with Heaviside functions only this upper bound can be overpassed, resulting in significant improvements of the solution, free of robustness issues.

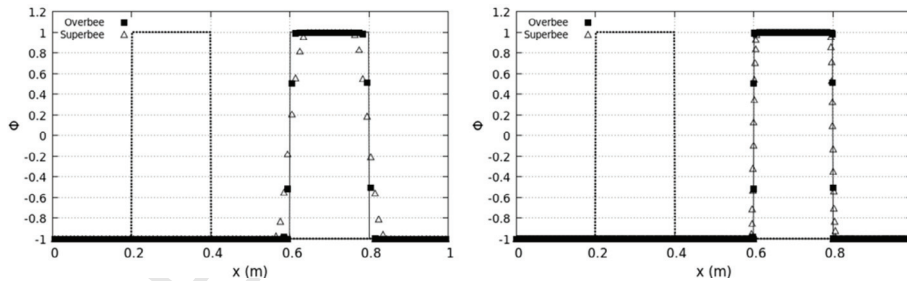


Figure 2.3- Comparison of the Overbee and Superbee limiters for the transport of a Heaviside function, here a Level-Set-type function. The advection speed is 100 m/s. The dashed lines represent the initial condition. The full line represents the exact solution. Gradients of the Heaviside function are computed with the least-squares method, corresponding in the one-dimensional case to central approximations. Final time: $t=4$ ms, CFL=0.8. On the graph at left 100 cells are used while on the one at right 1 000 cells are used. Overbee captures the discontinuity with two points only whatever the mesh resolution is.

In these computations, the gradients are computed with central approximations. Indeed, central differences correspond to the least-square approximation method that preserves accuracy and robustness in unstructured meshes codes (Barth and Jespersen, 1989). It appears that the Overbee limiter handles discontinuities in two points only for any mesh refinement and any method of gradient computation (central differencing as well as upwind-downwind). Its capabilities in multi-D are excellent as well, as shown in Fig. 2.4 where a Zalesak (1979) disc is transported at prescribed velocity (10 m/s) on an unstructured grid made of 16 156 triangles.

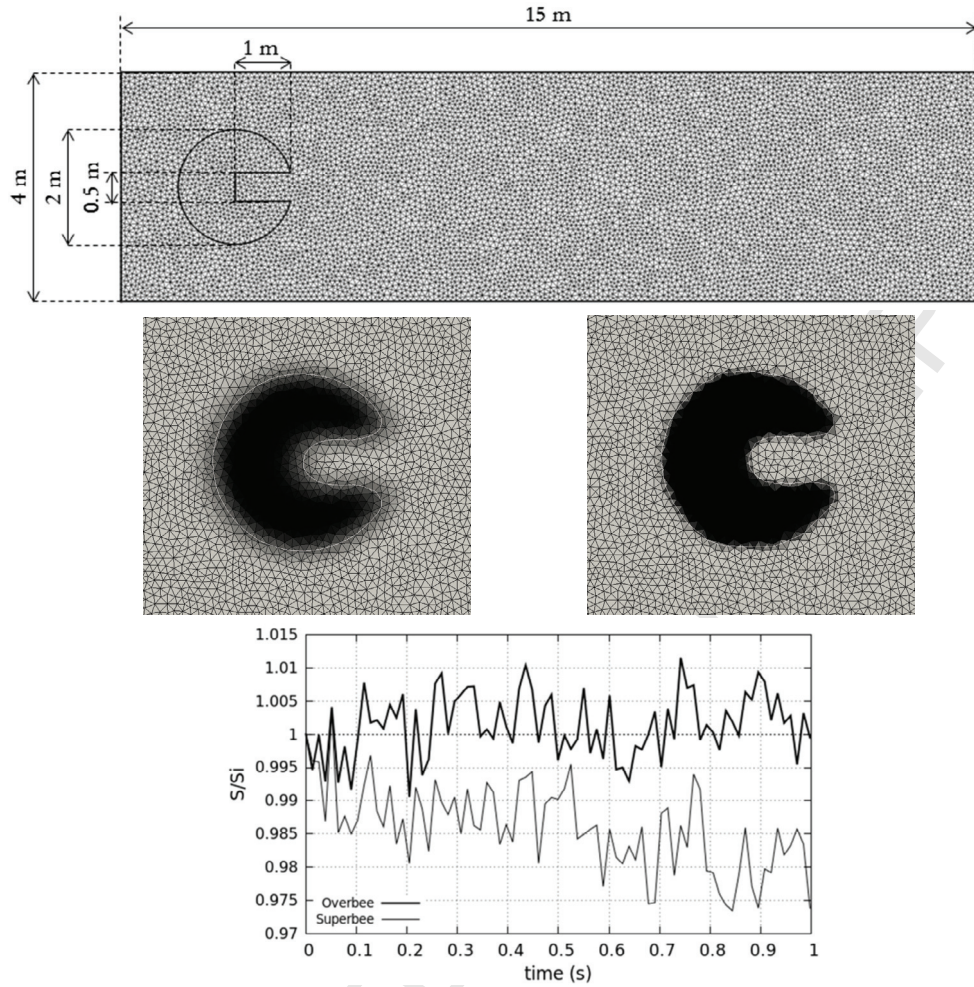
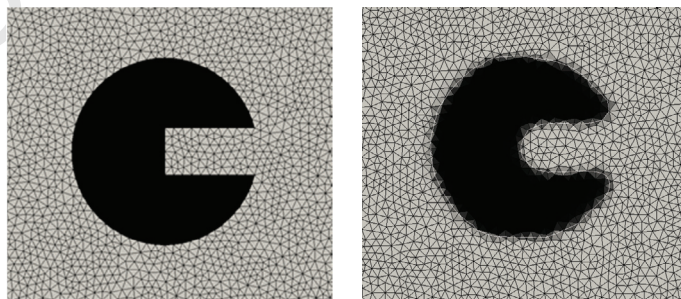


Figure 2.4- Transport of the Zalesak disc on an unstructured grid. The initial data and dimensions are shown on the upper graph.

Contours of the Level-Set function and its zero level are shown in the graphs at the middle, at time 1s, before exiting the right boundary of the domain. The graph at left is obtained with the MUSCL-Superbee scheme while the one at right uses Overbee.

The graph at bottom shows surface evolution. Superbee results in surface loss while Overbee preserves surface in the time average sense. All computations use least-square methods for the gradients computation, with an extended set of neighbors as defined in Fig. 2.6. The same mesh with 16 156 cells is used in both computations, corresponding to an average cell size of 0.05 m. The time step is computed to fulfil CFL restriction of 0.9.

The same computations are rerun on a bigger domain and the results are shown at times 1s, 2s and 3s with the MUSCL-Overbee method in Fig. 2.5.



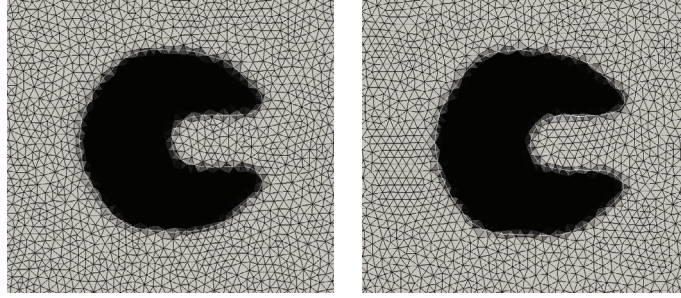


Figure 2.5- Transport of the Zalesak disc on an unstructured grid at times 0s, 1s, 2s and 3s with the MUSCL-Overbee scheme. The upper left graph corresponds to the initial shape of the Zalesak disc. The upper right graph represents the shape of the rigid body at time 1s. The bottom graphs represent respectively the Zalesak disc at time 2s at left and at time 3s at right. All computations use least-square methods for the gradients computation, with an extended set of neighbors as defined in Fig. 2.6. The average cell size is about 0.05 m. The time step is computed to fulfil CFL restriction of 0.9.

It appears that the overall shape is well preserved. It is worth to mention that the two stencils described in Fig. 2.6 have been considered for the gradients computation in the least-square method. The results are very similar, the final shape being slightly smoother with extended neighbors. Gradients computed with extended neighbors are always more accurate, having negligible extra cost in 2D computations and about 10% extra cost in 3D. These two stencils are illustrated in the Fig. 2.6.

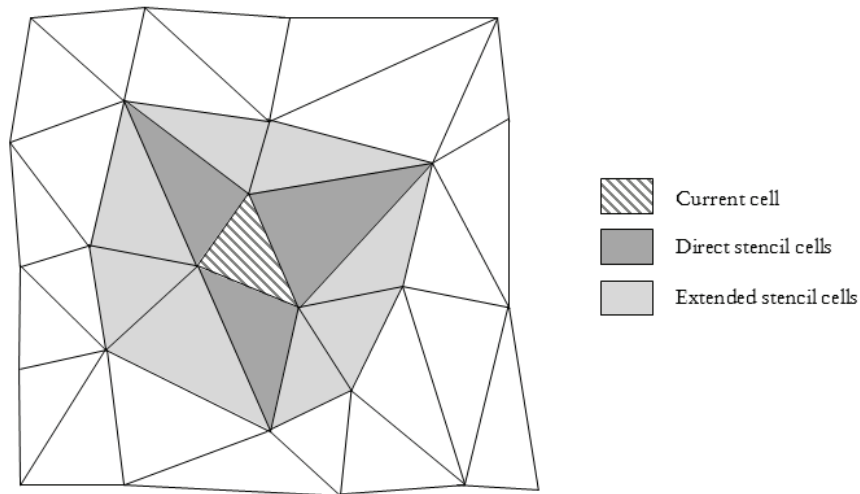


Figure 2.6- Definition of the two stencils: direct and extended neighbors.

Having now in hands a simple and efficient method to track rigid bodies, we now address coupling with the flow dynamics.

3 – Coupling methods

Solid-fluid coupling methods are now examined in the frame of a flow model that includes Euler and reactive Euler equations as well as multiphase mixtures in mechanical and thermal equilibrium. This formulation is particularly interesting to address phase transition at interfaces and in finely dispersed mixtures (Le Martelot et al., 2014, Saurel et al., 2016). In the present analysis, phase transition is omitted and coupling methods are analyzed in 1D.

3.1 – Flow model

The flow model, augmented by Level-Set equation reads,

$$\begin{aligned}
\frac{\partial \rho}{\partial t} + \bar{\nabla} \cdot (\rho \bar{\mathbf{u}}) &= 0 \\
\frac{\partial \rho \bar{\mathbf{u}}}{\partial t} + \bar{\nabla} \cdot (\rho \bar{\mathbf{u}} \otimes \bar{\mathbf{u}} + p \bar{\mathbf{I}}) &= \bar{\mathbf{0}} \\
\frac{\partial \rho E}{\partial t} + \bar{\nabla} \cdot ((\rho E + p) \bar{\mathbf{u}}) &= 0 \\
\frac{\partial \rho Y_k}{\partial t} + \bar{\nabla} \cdot (\rho Y_k \bar{\mathbf{u}}) &= 0 \\
\frac{\partial \Phi}{\partial t} + \bar{\nabla} \cdot (\Phi \bar{\mathbf{u}}_s) &= 0
\end{aligned} \tag{3.1}$$

In these notations index k represents a given fluid constituent (liquid or gas). ρ denotes the mixture density, $\bar{\mathbf{u}}$ and $\bar{\mathbf{u}}_s$ represent the velocity vector of the fluid and the solid respectively, Y_k represent the mass fraction constituent k and E the total energy of the fluid mixture ($E = \sum_k Y_k e_k + \frac{1}{2} \bar{\mathbf{u}} \cdot \bar{\mathbf{u}}$).

Each fluid is assumed to be governed by a convex equation of state (EOS). Here the stiffened-gas EOS is retained for each constituent as it represents reasonably the thermodynamics of liquids in limited ranges of temperature (typically 300-500K). It also includes the ideal gas EOS when some parameters are set to zero. For a given constituent it reads,

$$p_k = (\gamma_k - 1) \rho_k (e_k - q_k) - \gamma_k p_{k,\infty}, \tag{3.2}$$

where γ_k , q_k and $p_{k,\infty}$ are characteristic of a given constituent. A method to determine these parameters for liquid-vapor systems is given in Le Metayer et al. (2003). The stiffened-gas EOS can be improved to account for short distance repulsive effects, while remaining convex (Le Metayer and Saurel, 2016, Chiapolino and Saurel, 2018).

Under the assumption of temperature and pressure equilibrium among the phases, the following mixture EOS is obtained from the definition of mixture internal energy ($e = \sum_k Y_k e_k(T, p)$) and mixture specific

volume ($v = \sum_k Y_k v_k(T, p)$) definitions (Saurel et al., 2016):

$$p(\rho, e, Y_k) = \frac{\sigma + \sqrt{\sigma^2 + 4\bar{C}_v \omega}}{2\bar{C}_v} \quad \text{with} \quad \begin{cases} \sigma = \frac{e - \bar{q}}{v} (\bar{C}_p - \bar{C}_v) - p_{1,\infty} \bar{C}_v - p_{1,\infty} Y_1 (C_{p,1} - C_{v,1}) \\ \omega = \frac{e - \bar{q}}{v} p_{1,\infty} (\bar{C}_p - \bar{C}_v - Y_1 (C_{p,1} - C_{v,1})) \end{cases} \tag{3.3}$$

$$\text{and} \quad \bar{C}_v = \sum_{k=1}^N Y_k C_{v,k}, \quad \bar{C}_p = \sum_{k=1}^N Y_k C_{p,k}, \quad \bar{q} = \sum_{k=1}^N Y_k C_{v,k}.$$

The mixture temperature $T = T(\rho, p, Y)$ is obtained as,

$$T(\rho, p, Y_k) = \frac{1}{\rho \left(\sum_{k=1}^N \frac{Y_k (\gamma_k - 1) C_{v,k}}{p + p_{k,\infty}} \right)} \tag{3.4}$$

This EOS is valid when the liquid phase is denoted by index 1, the other constituents being ideal gases ($p_{k,\infty} = 0, k \neq 1$). It is worth to mention that when all constituents are ideal gases, the Dalton's law of ideal gas mixtures is recovered (Chiapolino et al., 2017). Therefore, System (3.1) with thermodynamic closure Eq. (3.3) can be used for single phase flows and two-phase liquid-gas mixtures in mechanical and thermal equilibrium.

System (3.1) is hyperbolic with the sound speed given in Le Martelot et al. (2014) page 65. However this formula is quite complicated and useless, as the Wood (1930) sound speed is simpler and slightly greater than the thermal and mechanical equilibrium sound speed. The Wood speed of sound is consequently a better candidate for numerical computations, with respect to CFL computation as well as wave speeds computation in approximate Riemann solvers. It is given by:

$$\frac{1}{\rho c^2} = \frac{1}{\sum_{k=1}^N \left[\frac{\alpha_k}{\rho_k c_k^2} \right]}, \quad (3.5)$$

where $\alpha_k = \frac{\rho Y_k}{\rho_k(T, p)}$ denotes the volume fraction of phase k.

In the limit of vanishing mass and volume fractions of the liquid phase and when a single gas constituent is present the Euler equations of gas dynamics are recovered. This remark enables building of a simple 1D reference solution to assess the accuracy of the various coupling methods.

3.2 – Reference solution

An immersed piston in a fluid, here the air considered as an ideal gas, is set to motion impulsively at time $t=0$. The impulsive motion to the right induces propagation of a right facing shock wave and a left facing expansion wave. A schematic (x,t) diagram is shown in Fig. 3.1 as well as qualitative profiles of velocity, pressure and density at a given time. This test problem is reminiscent of the exact Riemann problem solution except that the velocity between the two extreme waves is prescribed.

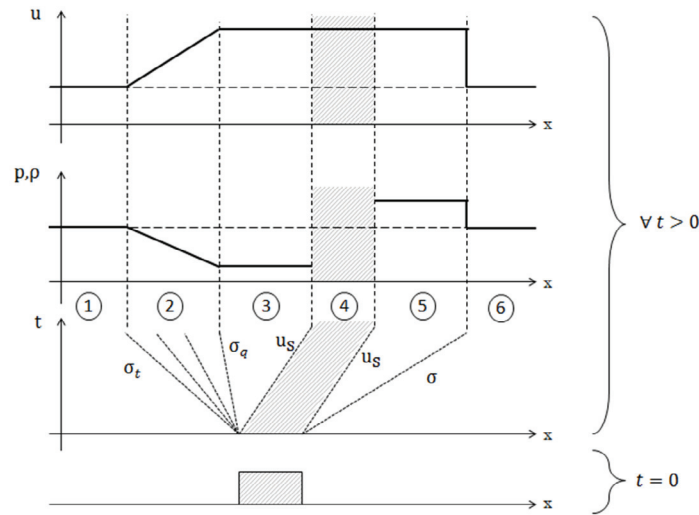


Figure 3.1- Immersed piston test problem. Schematic representation of the (x,t) diagram and associated velocity, pressure and density profiles.

The various states present in the solution are:

- (1) left state initially at rest,
- (2) expansion wave,
- (3) fully expanded fluid,
- (4) piston,

- (5) post shock state,
- (6) right state initially at rest.

The exact solution is straightforward. Knowledge of the piston velocity combined to the Rankine-Hugoniot relations determines fully state (5). The use of the Riemann invariants between state (1) and (3) where the velocity is the one of the piston determines fully state (3) and any point of the expansion wave (2). An example of such solution is given in Fig. 3.2 with initial data of Table 3.1.

Temperatures T_1 and T_6	293 K
Velocities u_1 and u_6	0
Pressures p_1 and p_6	100 000 Pa
Domain length	1 m
Initial position of the piston (m)	$0.4 \leq x \leq 0.5$
Velocity of the piston u_s	100 m/s
Final time	1 ms

Table 3.1- Initial data for the immersed piston test problem.

The air thermodynamics is modeled through EOS (3.2) with following data: $\gamma = 1.4$; $p_\infty = 0$ Pa; $q = 0$ J/kg.

The corresponding exact solution is shown in Fig. 3.2. These results will serve as reference for the three coupling methods that are considered hereafter.

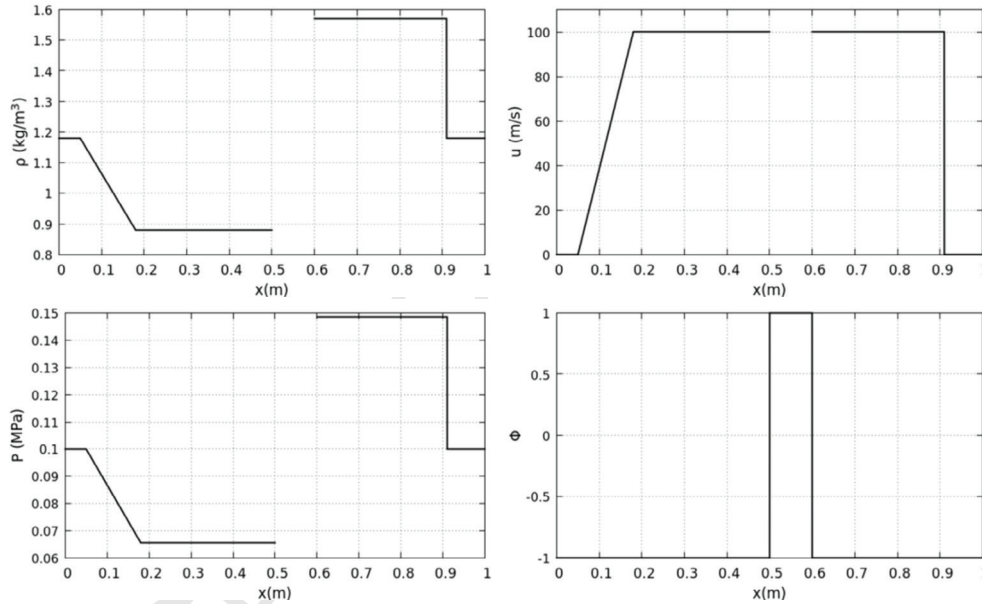


Figure 3.2- Exact solution for the immersed piston test problem moving in an ideal gas associated to initial data of Table 3.1.

3.3 – First coupling method: Velocity penalization

In the present paragraph the coupling method is studied in 1D and the flow model (3.1) is reduced to the Euler equations to facilitate both presentation and comparison with the former exact solution. Also, a single moving rigid body is considered. The corresponding flow model with stiff velocity relaxation (penalization) among the body and fluid reads,

$$\begin{aligned}
\frac{\partial \rho}{\partial t} + \frac{\partial \rho u}{\partial x} &= 0 \\
\frac{\partial \rho u}{\partial t} + \frac{\partial (\rho u^2 + p)}{\partial x} &= F_\Phi \\
\frac{\partial \rho E}{\partial t} + \frac{\partial (\rho E + p)u}{\partial x} &= F_\Phi \cdot u_s \\
\frac{\partial \Phi}{\partial t} + \frac{\partial \Phi u_s}{\partial x} &= 0
\end{aligned} \tag{3.6}$$

where F_Φ represents the drag force exerted by the fluid on the solid and $F_\Phi \cdot u_s$ the power of this force.

The coupling force is modelled as,

$$F_\Phi = \rho \frac{1 + \tilde{\Phi}}{2} \frac{u_s - u}{\tau} \tag{3.7}$$

where the relaxation time tends to zero ($\tau \rightarrow 0^+$) and factor $\frac{1 + \tilde{\Phi}}{2}$ makes this force present in the numerical diffusion zone of the solid-fluid interface, on the solid side only. Similar approach is examined in Abgrall et al. (2014).

The modified Level-Set function $\tilde{\Phi}$ is defined as:

$$\tilde{\Phi} = \begin{cases} +1 & \text{if } \Phi > 0 \\ -1 & \text{if } \Phi < 0 \end{cases} \tag{3.8}$$

This model is thermodynamically consistent as the entropy equation reads,

$$\frac{\partial \rho s}{\partial t} + \frac{\partial \rho s u}{\partial x} = \rho \frac{1 + \tilde{\Phi}}{2} \frac{(u_s - u)^2}{\tau} \geq 0 \tag{3.9}$$

In the stiff velocity relaxation limit, the production term vanishes, rendering the coupling method isentropic.

System (3.6) is solved by a splitting method, where the hyperbolic part is first solved with a MUSCL-type-scheme in the absence of source terms. The HLLC approximate Riemann solver of Toro et al. (1994) is used in all computations of the paper, to solve System (3.6) and its multi-D extension, System (3.1). The same equations are solved everywhere and the initial fluid state is set in the rigid body, except regarding the velocity, set to the one of the solid body. During this step, the Overbee limiter is used for the Level-Set function and another limiter (Minmod for example) is used for the other flow variables.

Second, the following ODE system is considered:

$$\begin{aligned}
\frac{\partial \rho}{\partial t} &= 0 \\
\frac{\partial \rho u}{\partial t} &= \rho \frac{1 + \tilde{\Phi}}{2} \frac{u_s - u}{\tau} \\
\frac{\partial \rho E}{\partial t} &= \rho \frac{1 + \tilde{\Phi}}{2} \frac{u_s - u}{\tau} \cdot u_s \\
\frac{\partial \Phi}{\partial t} &= 0
\end{aligned} \tag{3.10}$$

Rather than solving explicitly this ODE system, its asymptotic solution can be obtained easily as,

$$\rho = \rho^0; \Phi = \Phi^0; u = u_s, \tag{3.11}$$

where the superscript '0' denotes the variables determined at the end of the hyperbolic step. Update of the total energy only requires specific attention.

Manipulating the equations of System (3.10), the internal energy equation is obtained as,

$$\frac{\partial e}{\partial t} = \frac{1 + \tilde{\Phi}}{2} \frac{(u_s - u)^2}{\tau}$$

As $\tau \rightarrow 0^+$, asymptotic expansion of the source terms shows immediately, as for the entropy equation, that,

$$e = e^0.$$

But as the velocity has been reset to the rigid body one, as expressed by Eq. (3.11), the total energy has to be corrected as,

$$(\rho E) = \rho^0 \left(e^0 + \frac{1}{2} u_s^2 \right) \quad (3.12)$$

The coupling method thus consists in the reset of the velocity and the total energy with the help of Eqs. (3.11) and (3.12) in zones where $\Phi > 0$. This method is consequently particularly simple. It is tested in Fig. 3.3 on the immersed piston test case of Figs. 3.1-3.2.

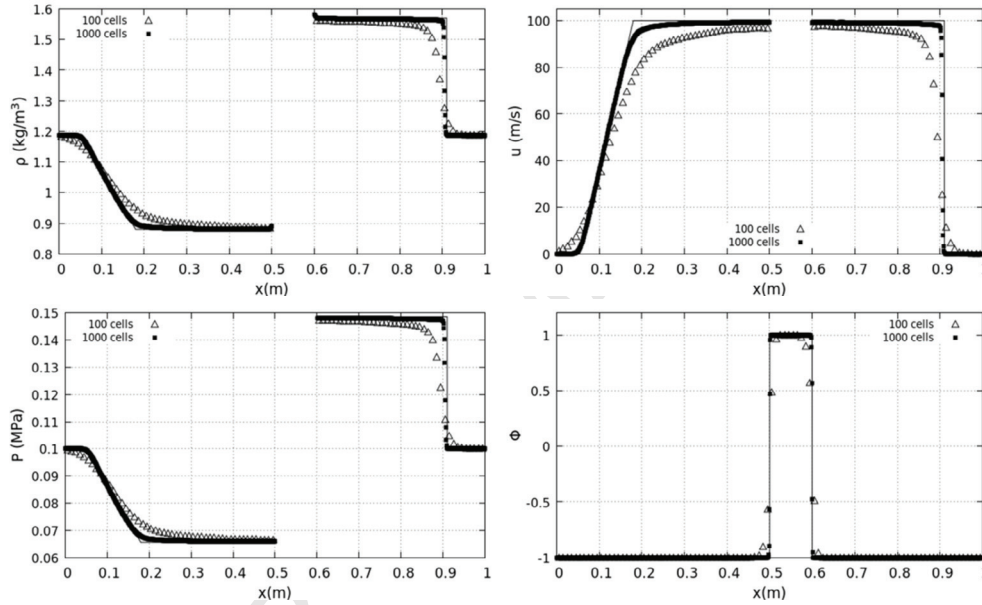


Figure 3.3- Relaxation method results. The first coupling method is used to compute the immersed piston test problem with two meshes, 100 and 1000 cells respectively and CFL=0.9. The Level-Set function is updated with the MUSCL-Overbee method while Minmod is used for the other variables. Numerical results are compared to the exact ones reported here in lines. Poor accuracy is obtained with 100 cells but the method tends to converge to the exact solution under mesh refinement.

This method converges to the exact solution, but the convergence rate seems slow. Another method, closer to the Ghost-Fluid-Method of Fedkiw et al. (1999) is thus addressed to improve convergence and efficiency.

3.4 – Second coupling method: Ghost-Cell-type method

In this second method, the hyperbolic step is unchanged and based on MUSCL-type-scheme with two limiters, as mentioned above. As in all computations the HLLC solver is used in the hyperbolic step. The coupling step is based on extrapolated variables from the fluid to the solid:

$$\begin{pmatrix} \rho_i \\ u_i \\ p_i \end{pmatrix} = \begin{pmatrix} \rho_j \\ u_s \\ p_j \end{pmatrix} \text{ if } \begin{cases} \Phi_i^0 \geq 0 \\ \Phi_j^0 < 0 \end{cases} \quad (3.13)$$

where i and j denote two neighboring cells, i being in the solid body and j in the fluid.

In Ghost-Cell (GC) methods the band of cells in which the extrapolation is done has importance. When extrapolation is done with System (3.13), interfacial cells only are corrected. But at the next time step the interface may leave the cell and enter another cell occupied formerly by the solid. This cell must consequently be filled with a consistent set of variables. This issue is illustrated in the Fig. 3.4.

Let us denote by W the set of primitive variables used during the extrapolation $W = (\rho, u, p)^T$ and U the associated set of conservative variables. The extrapolation is done in the solid cell on the graph on top at left. No precise state is prescribed in cell $i+2$. Then the Riemann problem is solved everywhere (graph at bottom) and during the time step, the interface changes cell. At the end of the time step cell $i+1$ is now a fluid cell but the state it contains is wrong, as the Riemann problem solution between cells $i+1$ and $i+2$ is wrong too. Therefore, at the next time step, when extrapolation is done from cell $i+1$ to cell $i+2$, a wrong state is copied and the solution diverges.

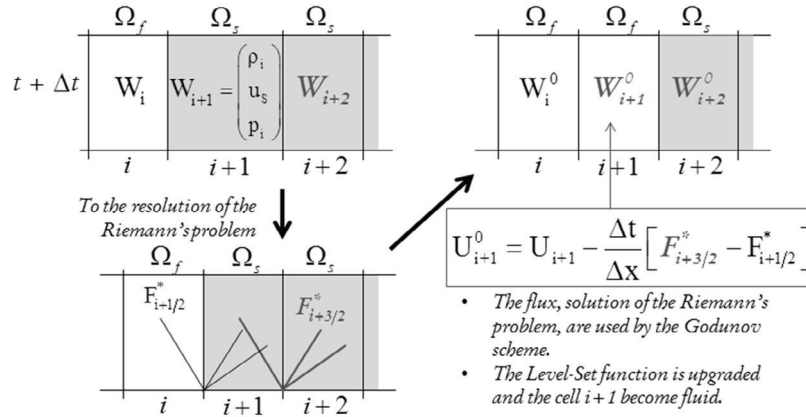


Figure 3.4- Schematic representation of the numerical pollution occurring when the extrapolation is done in a too narrow band of cells.

Typical results obtained with this numerical pollution effect are shown in the Fig. 3.5 where the same immersed piston test problem as before is rerun. Only the velocity graph is shown for the sake of conciseness.

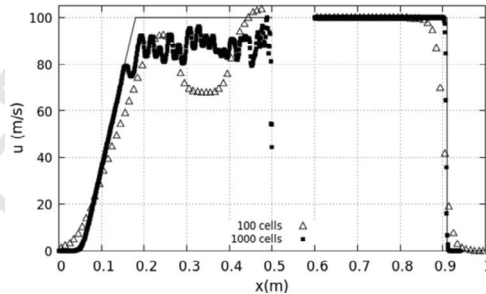


Figure 3.5- Illustration of the numerical pollution effect when a too narrow band of Ghost cells is used for extrapolation. The piston velocity is transmitted to the fluid on the right side but the expansion wave on the left side is wrong. This issue persists when the mesh is refined.

This issue is well known in the literature (Liu et al., 2003, 2006, 2008). Following these references the extrapolation method given by System (3.13) is extended to a band of two cells in the solid in the vicinity of the interface. The corrected algorithm is summarized in System (3.14):

$$\begin{cases} \begin{pmatrix} \rho_i \\ u_i \\ p_i \end{pmatrix} = \begin{pmatrix} \rho_j \\ u_s \\ p_j \end{pmatrix} \text{ if } \begin{cases} \Phi_i^0 \geq 0 \\ \Phi_j^0 < 0 \end{cases} \\ \begin{pmatrix} \rho_{ii} \\ u_{ii} \\ p_{ii} \end{pmatrix} = \begin{pmatrix} \rho_j \\ u_s \\ p_j \end{pmatrix} \text{ if } \begin{cases} \Phi_{ii}^0 \geq 0 \\ \Phi_j^0 < 0 \end{cases} \end{cases} \quad (3.14)$$

where i denotes the first solid cell in contact with the fluid cell j and ii the second solid cell, neighboring cell i . With this correction the immersed piston test is rerun and the results of Fig. 3.6 are obtained.

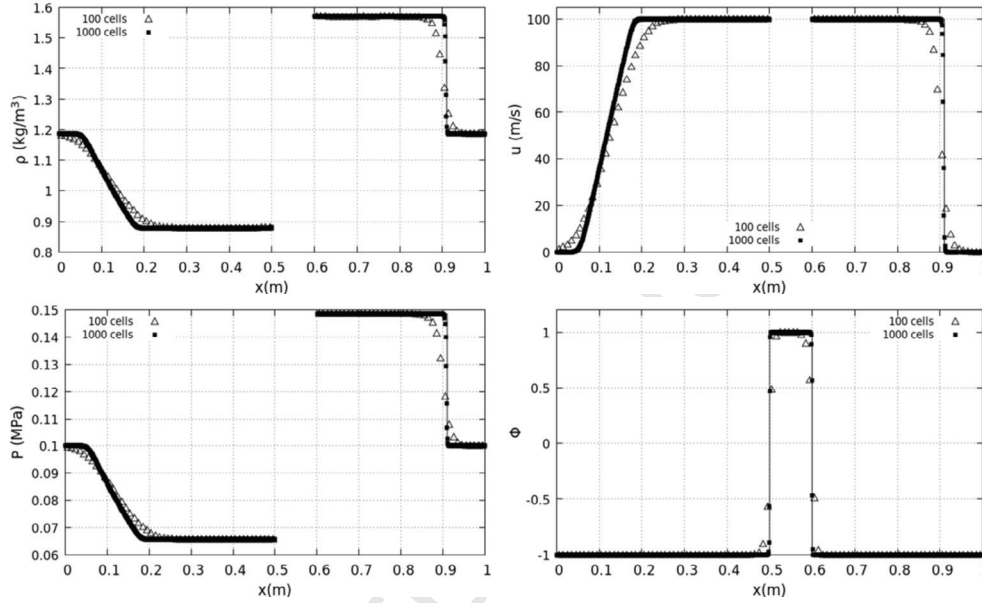


Figure 3.6- Ghost-Cell method with extended band of cells - Results for the immersed piston test. Two meshes are used with 100 and 1000 points respectively. The time step fulfills $CFL = 0.9$. The MUSCL scheme with Overbee is used for the Level-Set transport and Minmod is used for the other flow variables. The method converges to the exact solution shown in full lines under mesh refinement. With 100 cells, the accuracy is better than with the former relaxation method.

With the Ghost-Cell method summarized in System (3.14) interface conditions are matched for the two meshes considered. However, regarding the coarser one (100 cells) the shock is delayed compared to the exact solution of Fig. 3.2. The method improves efficiency compared to the relaxation one, but seems still perfectible. A refined version is examined in the next paragraph.

3.5 – Third coupling method: Ghost-Cell-type method with improved velocity extrapolation

The same Ghost-Cell-type method as before is considered, as summarized by System (3.14) but the extrapolated state is reconsidered in the aim of convergence improvement.

The present approach follows conventional method for the treatment of piston boundary conditions and avoids local resolution of exact or approximate Riemann problem, as done for example in Liu et al. (2006) and Farhat et al. (2012). It is thus aimed to simplify the related methods and facilitate coupling with more sophisticated flow models, as stated in the Introduction.

Let us consider a fluid at right and a solid at left. To mimic piston motion at prescribed velocity $u^* = u_{\text{piston}}$, where u^* denotes solution of the Riemann problem between two fluid states at left and at right, a fictitious state at left has to be determined. In this approach, the star state solution corresponds to the prescribed piston velocity. This approach is schematized in Fig. 3.7.

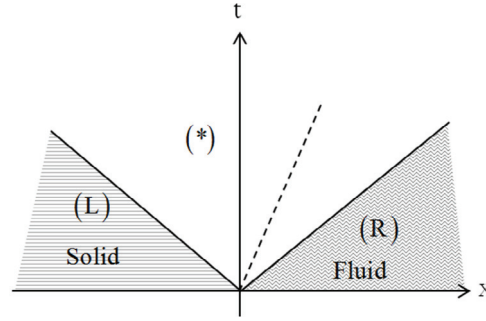


Figure 3.7- Schematic representation of the ‘inverse’ Riemann problem solved at the interface. The left state has to be determined in order that the star velocity becomes the one of the rigid body.

The right state (R) being known the left state (L) has to be determined in order that $\mathbf{u}^* = \mathbf{u}_{\text{piston}}$.

For the sake of simplicity in the analysis the approximate acoustic solver is considered:

$$\begin{cases} P_L + Z_L u_L = P^* + Z_L u^* \\ P_R - Z_R u_R = P^* - Z_R u^* \end{cases}$$

The pressure and density in the left state are assumed extrapolated from the right state, as done before with the former Ghost-Cell method. Consequently,

$$P_R = P_L = P; Z_L = Z_R = Z$$

The Riemann problem solution thus reads,

$$u^* = \frac{u_L - u_R}{2}; P^* = P + \frac{Z(u_L - u_R)}{2}$$

As $\mathbf{u}^* = \mathbf{u}_{\text{piston}}$ the left state velocity is determined as,

$$u_L = 2u_{\text{piston}} - u_R \quad (3.15)$$

It also appears that the pressure at the rigid body surface is,

$$P^* = P + Z(u_{\text{piston}} - u_R).$$

The term $Z(u_{\text{piston}} - u_R)$ induces compression or expansion depending on the sign of the velocity difference. In any case it anticipates shock or expansion appearance in the sense that it corresponds to the pressure, solution of the Riemann problem at the interface. However, there is no need to solve explicitly the Riemann problem locally. The HLLC solver (or any other flow solver) used to update the hyperbolic model will compute correctly the star pressure thanks to Eq. (3.15). Doing so, the present treatment provides the same solution as a multi-material or one-sided Riemann solver, without explicit consideration of such solver. Moreover, it is not limited to a specific EOS or a specific flow model.

Thanks to this correction, the extrapolation method, analogue of System (3.14) now reads,

$$\begin{cases} \begin{pmatrix} \rho_i \\ u_i \\ p_i \end{pmatrix} = \begin{pmatrix} \rho_j \\ 2u_s - u_j \\ p_j \end{pmatrix} \text{ if } \begin{cases} \Phi_i^0 \geq 0 \\ \Phi_j^0 < 0 \end{cases} \\ \begin{pmatrix} \rho_{ii} \\ u_{ii} \\ p_{ii} \end{pmatrix} = \begin{pmatrix} \rho_j \\ 2u_s - u_j \\ p_j \end{pmatrix} \text{ if } \begin{cases} \Phi_{ii}^0 \geq 0 \\ \Phi_j^0 < 0 \end{cases} \end{cases} \quad (3.16)$$

As before, i denotes the first solid cell in contact with the fluid cell j and ii the second solid cell, neighboring cell i . The immersed piston test problem is now rerun with this modification. Corresponding results are shown in Fig. 3.8.

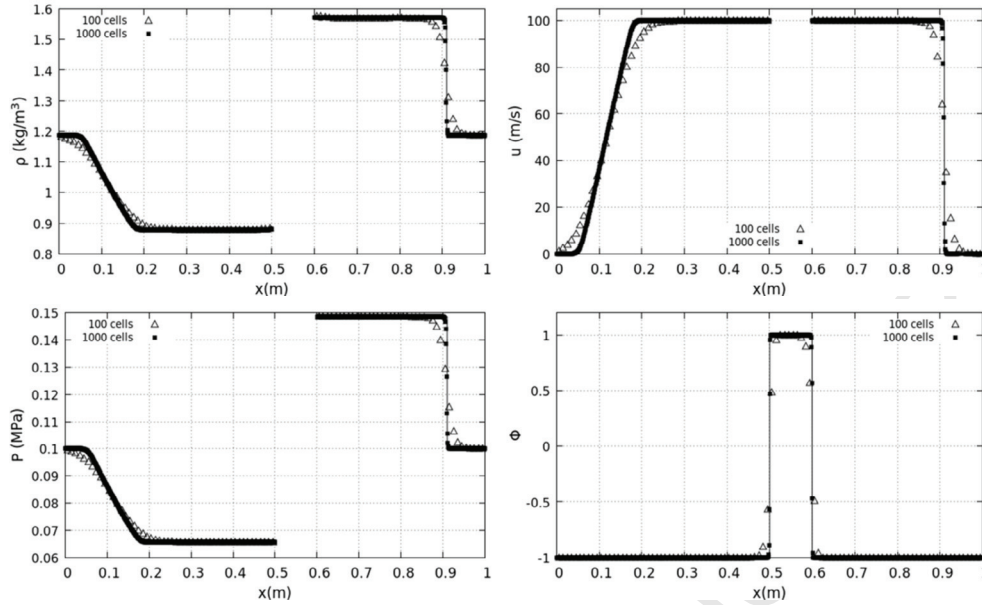


Figure 3.8- Ghost-Cell method with extended band of cells and modified boundary conditions - Results for the immersed piston test. Two meshes are used with 100 and 1000 points respectively. The time step fulfills $CFL = 0.9$. The MUSCL scheme with Overbee is used for the Level-Set transport and Minmod is used for the other flow variables. The method converges to the exact solution shown in full lines under mesh refinement. With 100 cells, the shock position is now correct.

The three coupling methods are now compared on the same graph with a coarse mesh involving 100 cells. Corresponding results are shown in Fig. 3.9.

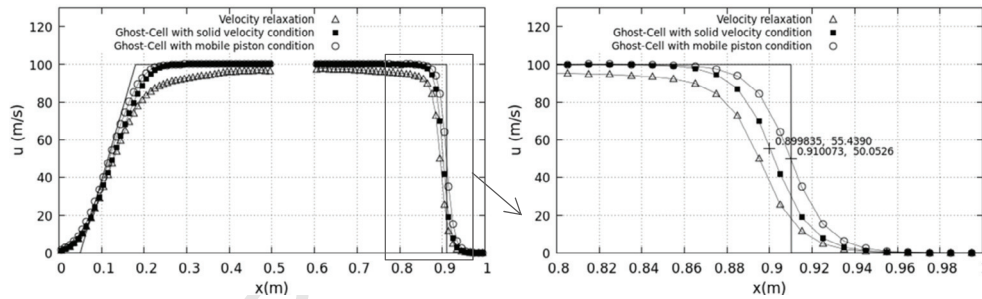


Figure 3.9- Comparison of the various coupling methods with 100 cells against the exact solution. The modified Ghost-Cell method with piston boundary condition improves the results.

We have shown that the three methods tend to converge to the exact solution, but the Ghost-Cell method with modified boundary condition improves the convergence rate. Let us now examine the method's behavior at various times, including very short ones. Corresponding results are shown in Fig. 3.10.

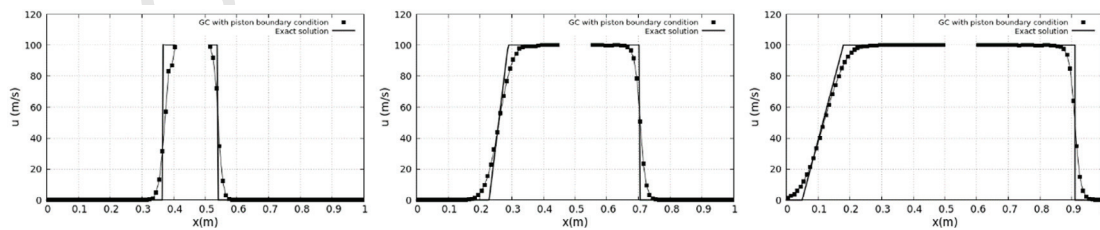


Figure 3.10- Efficiency of the coupling method at various times. Computations are done with 100 cells and compare to the exact immersed piston solution. The modified Ghost-Cell method with piston boundary condition is used in all computations. From the left to the right solutions have been plotted at times 0.1ms, 0.5ms and 1ms. It corresponds to 7, 28 and 53 time steps respectively. The coupling method matches the exact solution, even at short times with similar efficiency as simple phase Euler computations, needing 5 to 10 time steps to build shocks and expansion waves.

The modified Ghost-Cell method with piston boundary condition converges fast towards the exact solution for different times. At short times, waves' speeds are well computed and shocked state is quasi-formed. As time increases, the convergence of the solution is clear. We now address extension of this last method in multi-D on unstructured meshes.

4 – Multidimensional extension

The coupling method is now extended to multi-D. Transport of the Level-Set function in multi-D follows the lines of Chiapolino et al. (2017) regarding the volume fraction transport of their diffuse interface flow model. Therefore, it is not detailed anymore.

4.1 – Solid-fluid coupling method

Mixed cells have to be defined and to do this solid cells have to be defined first. As already mentioned a cell is considered solid when the Level-Set function Φ is positive at the cell center and fluid otherwise. It becomes a mixed cell when one of its direct neighbors has Φ with opposite sign, as shown in Fig. 4.1. It is worth mentioning that none of the fluid cells ($\Phi < 0$) are considered as mixed and are solved with the hyperbolic solver routinely. Thus mixed cells are defined as solid one ($\Phi > 0$) that share an edge with at least one fluid cell ($\Phi < 0$).

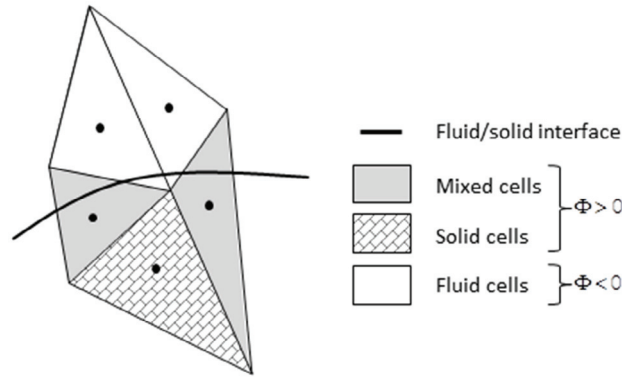


Figure 4.1- Schematic representation of the interface and mixed cells.

2D extension of the Ghost-Cell method proceeds in two-steps.

a) Approximation of the fluid state in mixed cells

When a mixed cell is detected the fluid state in the corresponding cell is computed as a volume average of the neighboring fluid cells. This average is obviously based on conservative variables.

Let's define Ω_{vf} the set of neighboring fluid cells of the considered mixed cell. The set of conservative variable in the mixed cell is obtained as,

$$\bar{\mathbf{U}} = \frac{\sum_{k \in \Omega_{vf}} V_k \mathbf{U}_k}{\sum_{k \in \Omega_{vf}} V_k}, \quad (4.1)$$

where V_k represents the volume of cell k . From this vector of conservative variables, primitive ones are deduced :

$$\tilde{\mathbf{W}} = \left(\tilde{\rho}, \tilde{u}, \tilde{v}, \tilde{p} \right)^T \quad (4.2)$$

Symbol \sim is used to make distinction with the volume average symbol.

These primitive variables are used during the extrapolation step that follows.

b) Extrapolation across the interface

The same piston boundary conditions are used in the direction normal to the solid-fluid interface. As the flow model (3.1) is inviscid the tangential velocity has to be extrapolated as well.

Let's consider two cells having a common edge and having Level-Set functions of different signs. Necessarily the interface I crosses the line segment connecting the two cell centers, as shown in Fig. 4.2 where the cell center containing a fluid state is denoted by F , the one containing a solid is denoted by G and the interface point is denoted by S .

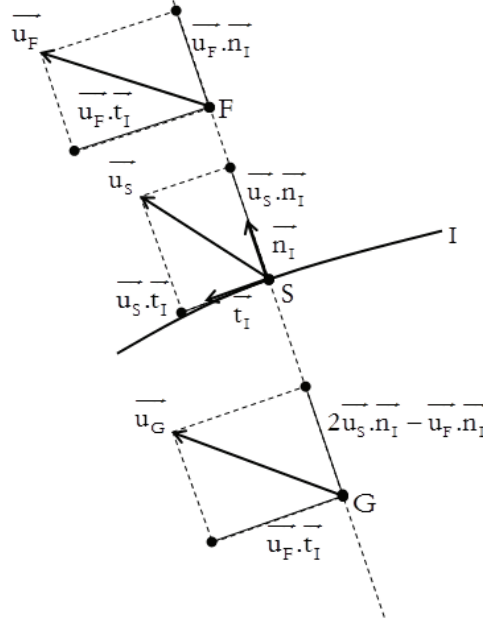


Figure 4.2- Schematic representation of construction of the velocity in the Ghost-Cell G when two mesh points have a common edge and Level-Set function changes sign. The normal velocity component in the Ghost-Cell is computed with both fluid and solid velocities contributions. The tangential component of the velocity at point G is taking equal to the tangential component of the fluid velocity, to mimic slip condition. Velocity at point G is determined following Eq. (4.3).

The normal vector to the interface is defined as,

$$\vec{n}_\Phi = -\frac{\vec{\nabla}\Phi}{\|\vec{\nabla}\Phi\|}$$

where $\vec{\nabla}\Phi$ is computed in each cell as mentioned in Section 2 with the least-square method and extended set of neighbors. The normal vector used in the extrapolation procedure is the one computed in the mixed cell, as defined earlier.

The velocity components are extrapolated in the solid as,

$$\vec{u}_G \cdot \vec{n}_I = 2\vec{u}_S \cdot \vec{n}_I - \vec{u}_F \cdot \vec{n}_I \quad \text{and} \quad \vec{u}_G \cdot \vec{t}_I = \vec{u}_F \cdot \vec{t}_I \quad (4.3)$$

along the normal and tangential directions respectively.

The rest of the primitive variable vector is copied in the solid cell.

c) Extrapolation to the Ghost-Cell band

As previously mentioned in the 1D case and comments related to Fig. 3.5 additional cells need to be filled with consistent fluid states. Indeed, at the next time step the interface may move away from the current cell and a solid cell may become a fluid one. The extrapolation procedure is

extended to a wider stencil to anticipate appearance of extra fluid cells. The ‘additional cells’ where a fluid state has to be defined are shown in Fig. 4.3. They are defined as solid cells having a mixed cell as direct neighbor.

A conservative average is performed with the neighboring mixed cells (also defined in Fig. 4.3), that have been updated with the sequence (4.1-4.2-4.3).

An extra conservative average is done on the mixed cells with the same definitions as Eqs. (4.1)-(4.2) *where the mixed-cells volumes and states are used instead of the fluid ones*. The resulting volume average done with the mixed cells is used to update the ‘additional cells’.

Two sequences of volume averages are consequently done with the present method:

- First with the fluid cells to update the mixture cells;
- Second with the mixture cells to update the ‘additional cells’.

Between these two averaging steps the piston boundary condition (4.3) is obviously used.

This simple averaging-extrapolation method simplifies significantly existing solid-fluid coupling methods on unstructured meshes.

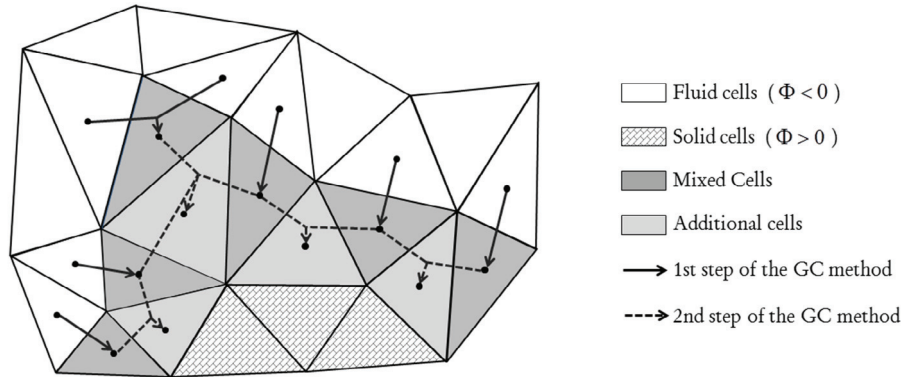


Figure 4.3 - Treatment of the Ghost-Cell band in 2D. All grey cells and hatched ones represent solid cells. These solid cells are divided in 3 categories. The first one, in dark grey, corresponds to the mixed cells in which extrapolation is done following (4.3) after volume average (4.1)-(4.2). The second layer, shown in grey, corresponds to the solid direct neighbors of the mixed cells, as defined in Figure 3.4. Fluid state is set in these cells by averaging conservative variables of the surrounding mixed cells with the help of (4.1)-(4.2) definitions. States and volumes of mixed-cells are used in these formulas. The third one with hatched symbols corresponds to the solid cells that are not modified by the coupling method.

To examine accuracy of the method reference results are determined, as detailed in the next subsection.

4.2 – Validation

In order to validate the treatment done in the coupling method for multidimensional problems, two computations are considered and compare. In one case, a supersonic flow at Mach number two enters a domain where a cylinder at rest is placed, as shown in Fig. 4.4(a). The results of this test are compared to the case where the cylinder moves at the same velocity as the inlet flow in a fluid at rest, as shown in Fig. 4.4(b). Results are compared at two different times. The flow model (3.1) is used in the single phase limit, corresponding to the Euler equations, with polytropic coefficient $\gamma_{\text{air}} = 1.4$.

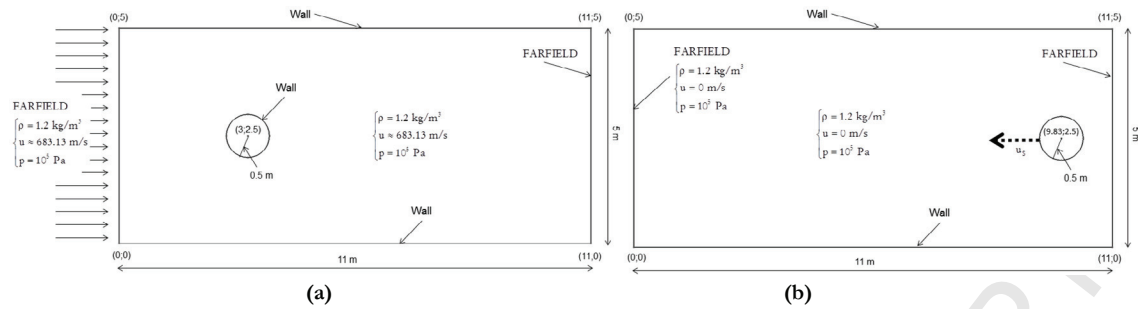


Figure 4.4- Configurations considered for validation of the coupling method in 2D. (a): A body fitted mesh is used around a cylinder at rest with a supersonic inflow at Mach number two. (b): The same cylinder moves at supersonic speed in a gas flow at rest.

The mesh density is taken with an average space size of 3 cm and Minmod limiter is used for the various flow variables in the MUSCL scheme.

Comparison of computed results is shown in Fig. 4.5 at times 2ms and 4ms respectively.

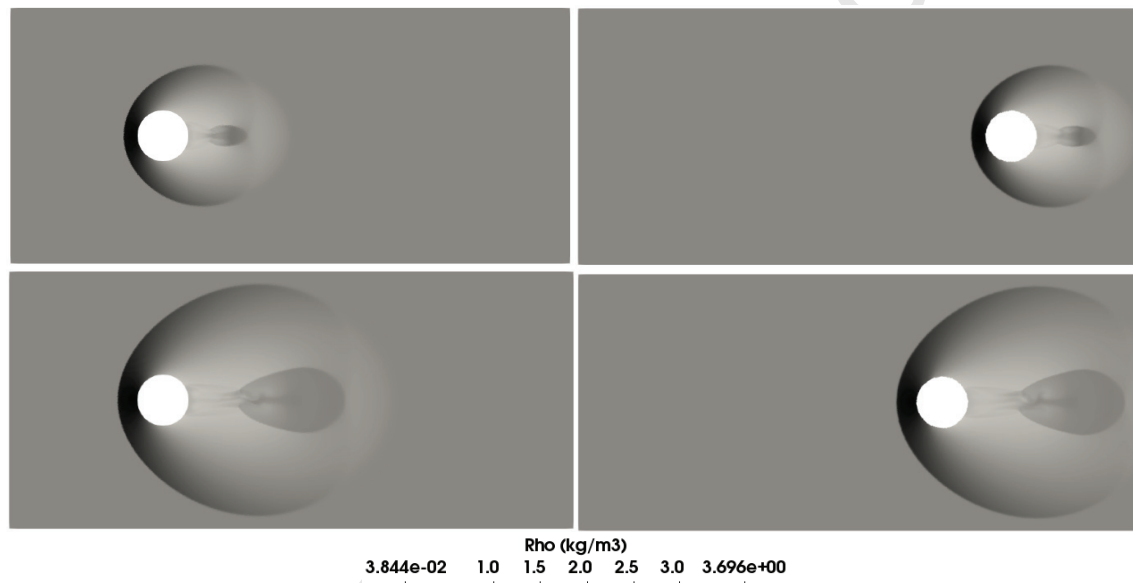


Figure 4.5- Comparison of the results with body at rest (left column) and moving body (right column) related to the configurations depicted in Figs. 4.4. The Minmod limiter is used in the MUSCL scheme. Upper graphs represent density contours at time 2ms while the lower graphs correspond to the solution at time 4ms. Good agreement is observed between the body-fitted approach and the coupling one.

The mesh of the geometry presented in Fig. 4.4(a) is composed of 202 716 cells corresponding to an average space step of 3 cm. The mesh of the geometry shown in Fig. 4.4(b) is composed of 205 628 cells corresponding to the same space step. Computed results of Fig. 4.5 are in close agreement. First the same detached shock wave is visible as well as expansion zone at rear of the projectile. Second, the shape of the projectile is very well preserved by the Level-Set-Overbee method. Last, it is possible to address quantitative comparison by extracting flow variables from the two sets of results along a given direction, such as the Ox axis for instance. This is done in Figs. 4.6 and 4.7 for the flow variables profiles respectively at time 2ms and 4ms.

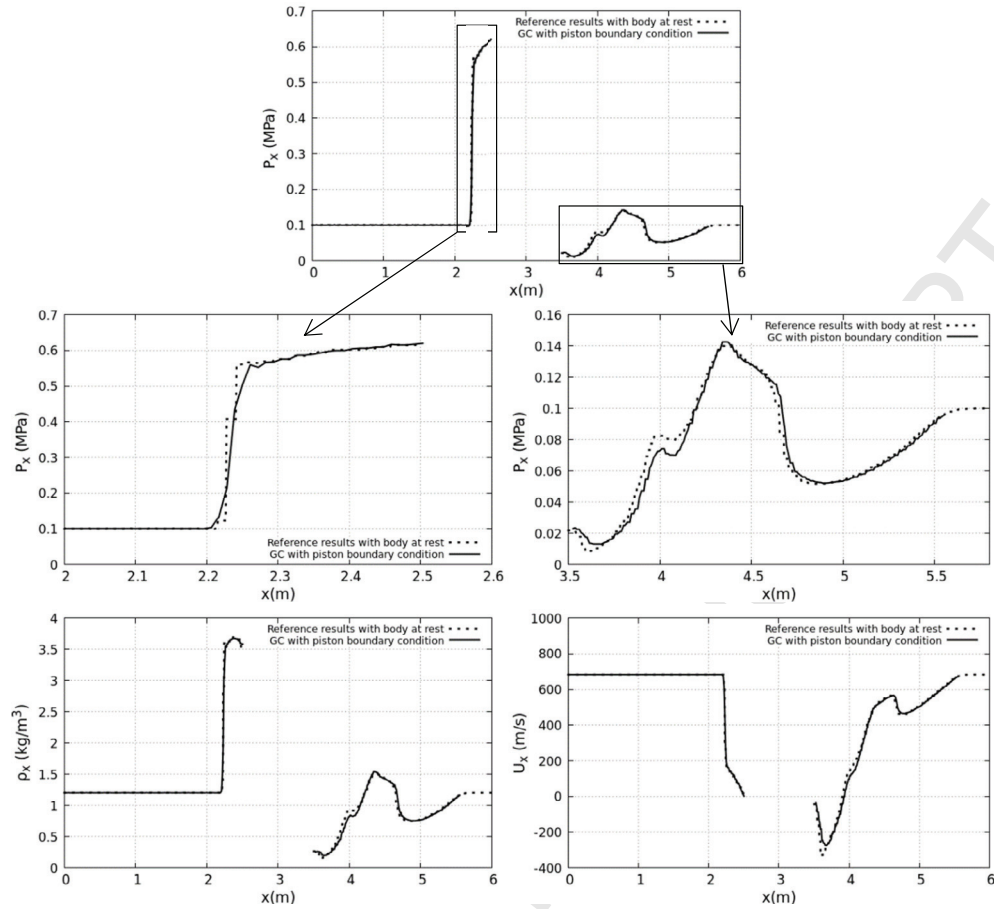


Figure 4.6- Comparison of the variables profiles along the Ox axis related to the computation of Fig. 4.5, at time 2ms. The range of X -axis has been modified in the moving body computations to compare the results with those related to body at rest. The velocity has been modified to represent relative velocity, for the same reason. Good agreement is observed.

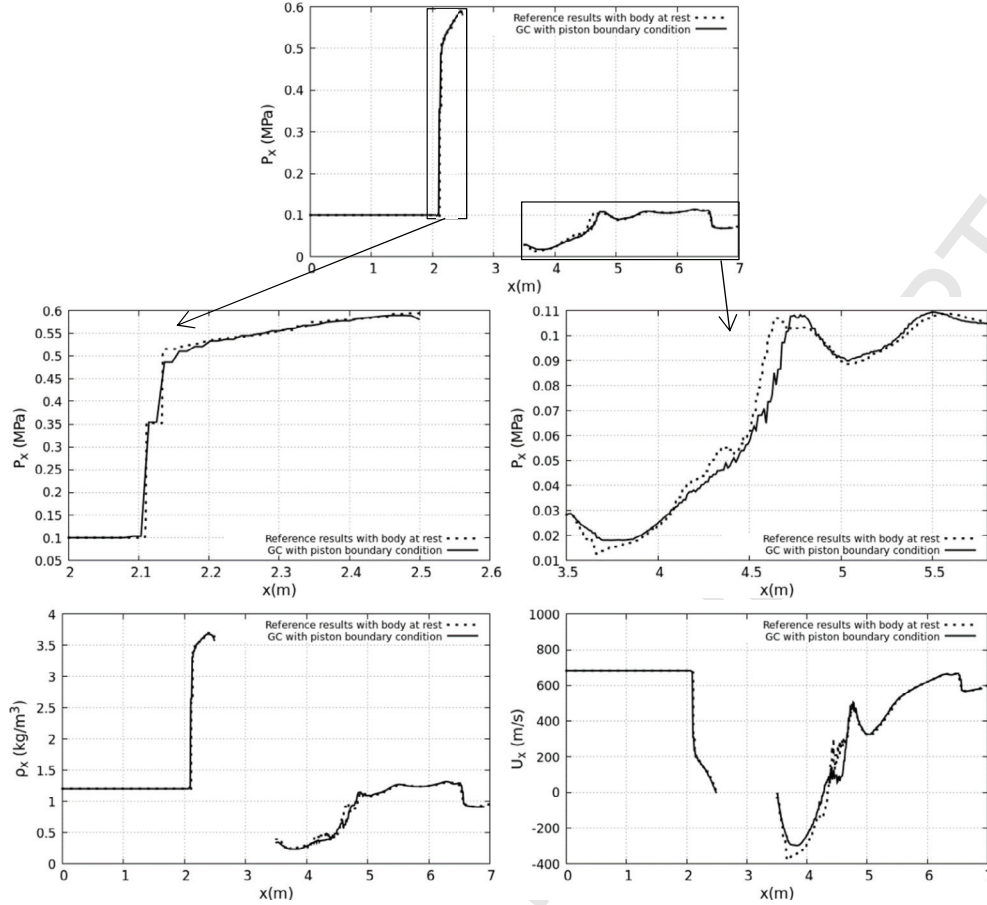


Figure 4.7- Comparison of the variables profiles along the Ox axis related to the computations of Fig. 4.5, at time 4ms. Good agreement is observed.

The results of Figs. 4.6 and 4.7 confirm validity of the coupling method with comparable accuracy as the one observed in 1D in the Figs. 3.10. The various profiles do not match perfectly as the meshes are not the same. Also, body roughness effects are present in the moving body computations. Overall agreement is good and the method remains simple to implement. Illustrations of the method's capabilities in the frame of the two-phase flow model (3.1) are now addressed.

4.3 – Illustrations with two-phase flow effects

Two projectiles of 5 mm radius with imposed velocities are considered and move at high velocity through air and impact a liquid water domain settled in the air. The air is considered as an ideal gas and the liquid is assumed governed by the stiffened gas EOS (3.2). As material interfaces between the various fluids are present the flow model (3.1) with mixture EOS (3.3) is an appropriate candidate, in particular when phase transition is considered (Saurel et al., 2016). Thermodynamic data of the various fluids are given hereafter:

$$\begin{cases} \gamma_{w,liquid} = 2.35 ; p_{\infty,w,liquid} = 10^9 \text{ Pa} ; q_{w,liquid} = -1167 \text{ kJ/kg} ; C_{v,w,liquid} = 1816 \text{ J/kg/K} \\ \gamma_{w,vapor} = 1.43 ; p_{\infty,w,vapor} = 0 \text{ Pa} ; q_{w,vapor} = 2030 \text{ kJ/kg} ; C_{v,w,vapor} = 1040 \text{ J/kg/K} \\ \gamma_{air} = 1.4 ; p_{\infty,air} = 0 \text{ Pa} ; q_{air} = 0 \text{ J/kg} ; C_{v,air} = 719 \text{ J/kg/K} \end{cases}$$

Phase transition is considered through local thermodynamic equilibrium. Simple and fast thermochemical relaxation solver has been developed in Chiapolino et al. (2017) and is used in the present computations. Initial and boundary conditions are given in the Fig. 4.9 as well as geometrical data.

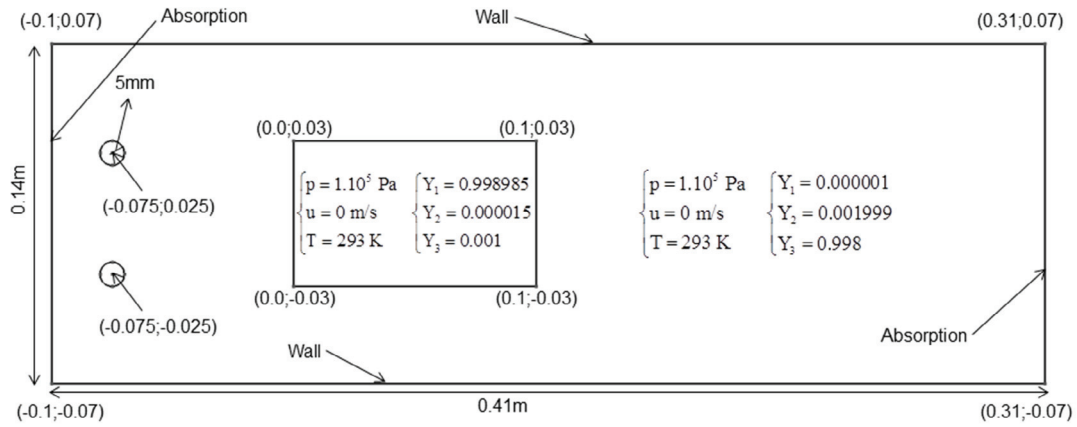


Figure 4.9- Projectiles impact at high velocity onto a water tank in the air. Geometrical data and initial and boundary conditions. The upper projectile has initial velocity components (400, -10) while the lower one has (400, +10) in m/s units.

Corresponding computational results are shown in Fig. 4.10 at several times.

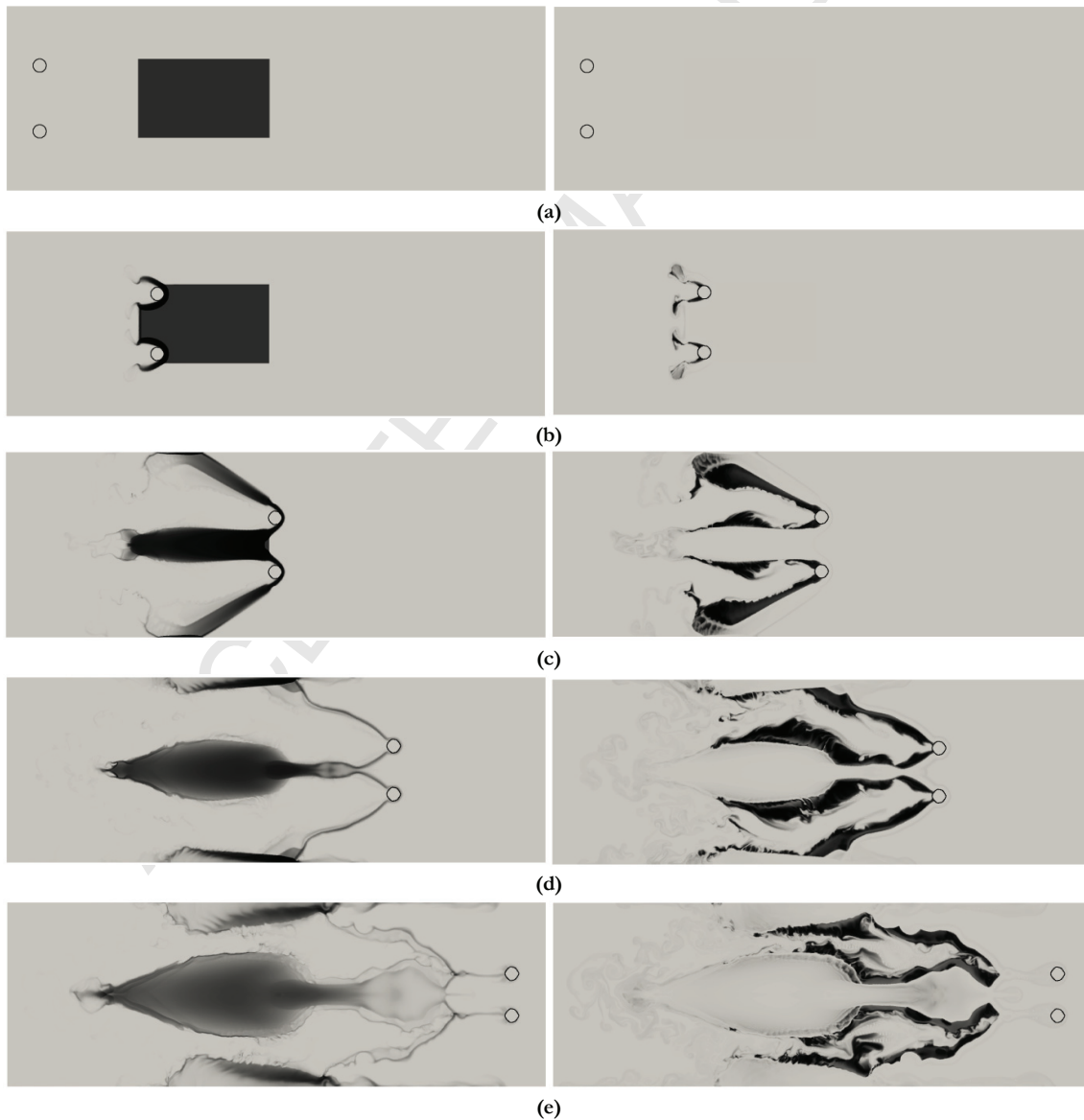




Figure 4.10- Interaction of two projectiles at high speed on a water tank settled in the air. Computed volume fractions of liquid water (left column) and water vapor (right column) appearing during cavitation. Computational parameters: MUSCL scheme with Overbee limiter for the Level-Set functions, Minmod limiter for the other variables, CFL = 0.5, number of cells (triangles) = 1 489 476. Results are shown at times (a) 0 ms ; (b) 0.225 ms ; (c) 0.45 ms ; (d) 0.675 ms ; (e) 0.9 ms.

Fig. 4.10 illustrates method's capabilities where two-phase effects with phase transition are present, in the presence of liquid gas interfaces and solid-fluid interfaces. These computations show that vapor is produced during the impact and travel of the projectiles in the two-phase cloud. Vapor is produced at approximately 135° from the stagnation point. The related vapor volume fraction is high in this example as it reaches nearly 1 at some locations. Extra extension is now addressed with two-way coupling.

5 – Two-way coupling

The motion of rigid bodies is now considered as coupled to the fluid flow through the pressure force integral over the body surface. The pressure force exerted by the fluid on the solid surface is defined as,

$$\vec{F}_p = \int_{\partial\Omega_s} p \vec{n} dS = F_{px} \vec{e}_x + F_{py} \vec{e}_y \quad (5.1)$$

where $\partial\Omega_s$ denotes the surface of the rigid body.

The cell faces belonging to the rigid boundary surface are detected as:

- For a given face 'f' belonging to the entire set of faces of the overall mesh. This face belongs to two neighboring cells, say for instance cells i and j.
- If the product of the Level-Set functions $\Phi_i \cdot \Phi_j < 0$, then the face belongs to the set of faces of $\partial\Omega_s$.

Consequently the discrete analogue of Eq. (5.1) becomes,

$$\vec{F}_p = \sum_{f \in \partial\Omega_s} p_f \vec{n}_f S_f \quad (5.2)$$

With the help of pressure force exerted on the rigid body its velocity is updated thanks to the Newton's law:

$$\vec{u}_s^{n+1} = \vec{u}_s^n + \Delta t \frac{\vec{F}_p}{M} \quad (5.3)$$

As the rigid body velocity is time dependent but independent of space, the Level-Set function still obeys the conservation law, Eq. (2.3). The overall algorithm described in Sections 3 and 4 is thus unchanged.

The method is now illustrated on various flow configurations. An array of 6 cylindrical particles of radius $r = 5$ mm is considered and set to motion under shock wave interaction. The mass of each particle is arbitrarily set to $M=0.8$ g and are initially settled in air at atmospheric conditions. Each particle is tracked by its own Level-Set function, different for each particle. At the left boundary of the domain, piston conditions are adopted corresponding to a shock wave emitted to the gas at Mach number 1.24. The various initial and boundary conditions are given in Fig. 5.1. In the first run, the particles are aligned.

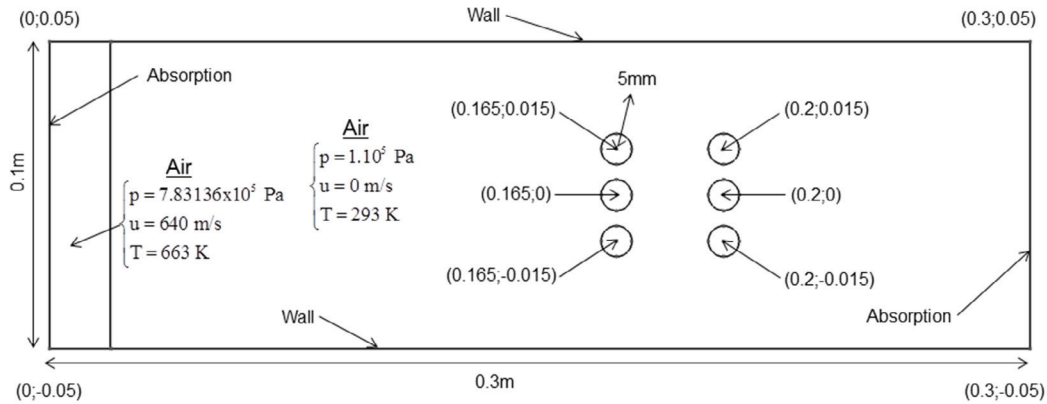


Figure 5.1- Two-way coupling illustration 1 – Shock interaction with an array of aligned particles. Initial data and boundary conditions.

As before, the MUSCL scheme is used with Overbee limiter for the Level-Set function and Minmod for the other flow variables. The pressure contours resulting of the shock interaction are shown at various times in the Figure 5.2.

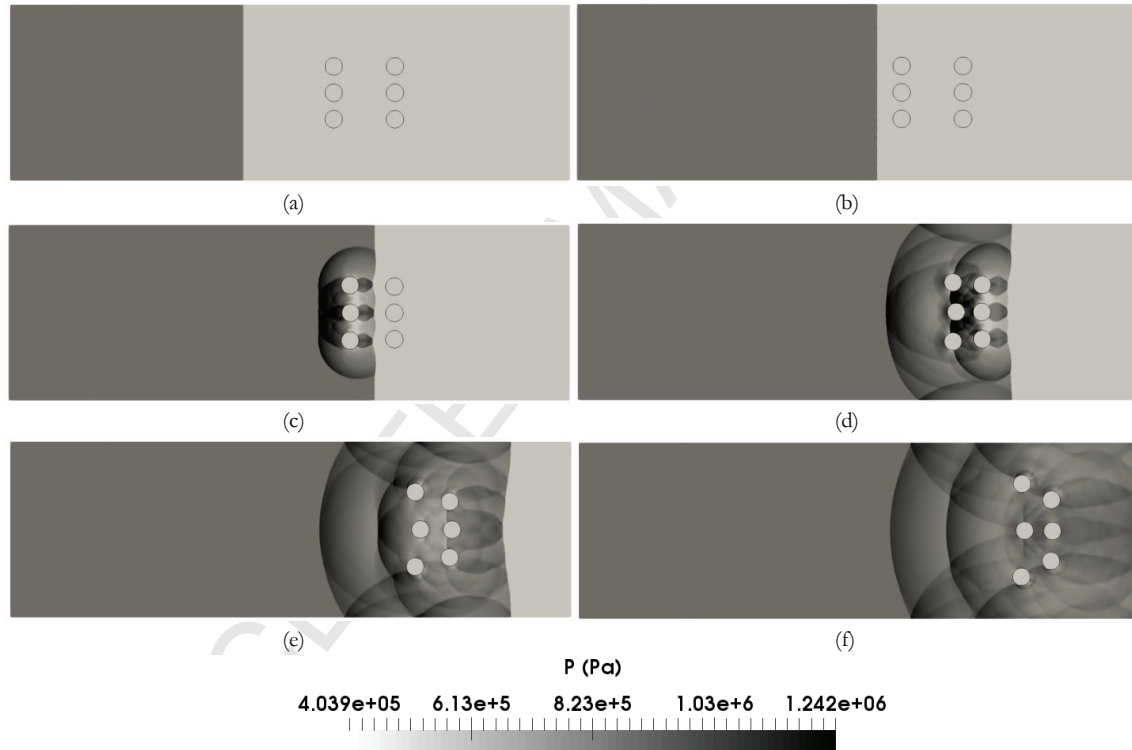


Figure 5.2- Pressure contours resulting of the shock interaction with an array of aligned rigid solid particles. The mesh involves 615 278 cells corresponding to an average space size of 0.2 mm. Both transmitted and reflected shock waves are clearly visible as well as the motion of the various particles, no longer aligned during time evolution. The results are shown at times (a) 0.126 ms ; (b) 0.168 ms ; (c) 0.21 ms ; (d) 0.252 ms ; (e) 0.294 ms ; (f) 0.336 ms.

At each interaction with a particles layer a reflected shock is emitted. Indeed, after the passage of the first particles layer, the shock reforms very quickly and interacts with the second layer, resulting in both transmitted and reflected shock waves. The transmitted shock reforms quickly to a discontinuous wave, while the reflected one stays a train of shock waves during the physical time observed.

It is interesting to note the very good symmetry of the computations while achieved on unstructured grids, this observation giving confidence to the coupling method.

The same type of initial configuration with staggered particles is considered for a second run, as shown in Fig. 5.3.

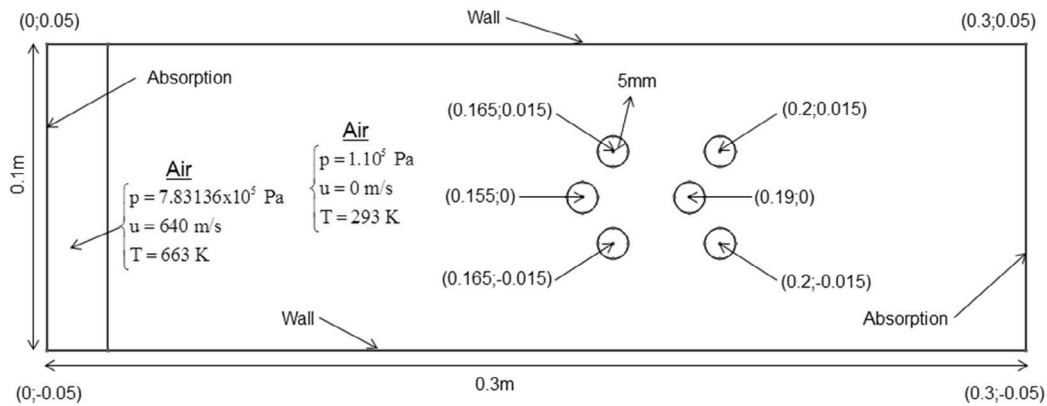


Figure 5.3- Two-way coupling illustration 2 – Shock interaction with an array or staggered particles. Initial data and boundary conditions.

Associated computational results are shown in Fig. 5.4.

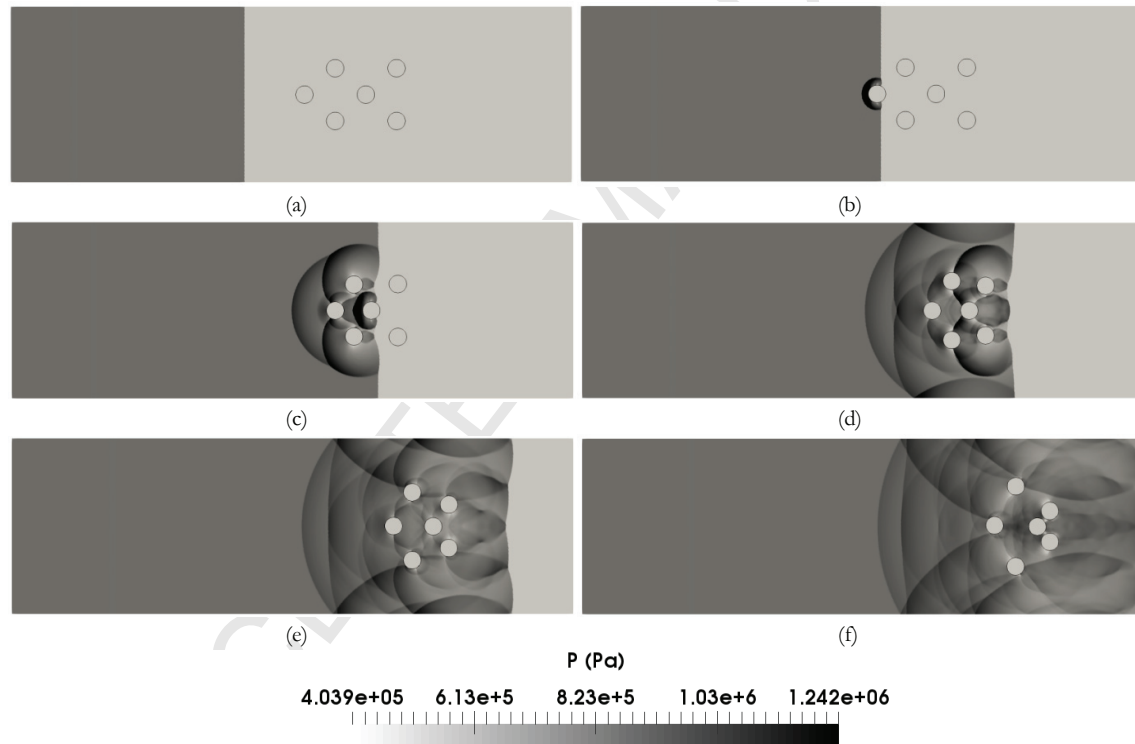


Figure 5.4- Pressure contours resulting of the shock interaction with an array of staggered rigid solid particles. The mesh involves 616 454 cells corresponding to an average space size of 0.2 mm. Both transmitted and reflected shock waves are clearly visible as well as the motion of the various particles that tend to form a cluster. The results are shown at times (a) 0.126 ms ; (b) 0.168 ms ; (c) 0.21 ms ; (d) 0.252 ms ; (e) 0.294 ms ; (f) 0.336 ms.

The same observations as for the previous test are valid. An extra interesting feature appears with the particle layer at right that tends to form a cluster due to the interactions with the fluid flow.

Mesh sensitivity dependence of the results is investigated hereafter. Three meshes are considered : a very coarse one made of 40 222 cells, an intermediate one made of 158 680 cells, a refine one made of 610 454

cells and a very fine one made of 2 424 922 cells. The same computational parameters of the MUSCL and coupling methods as before are used.

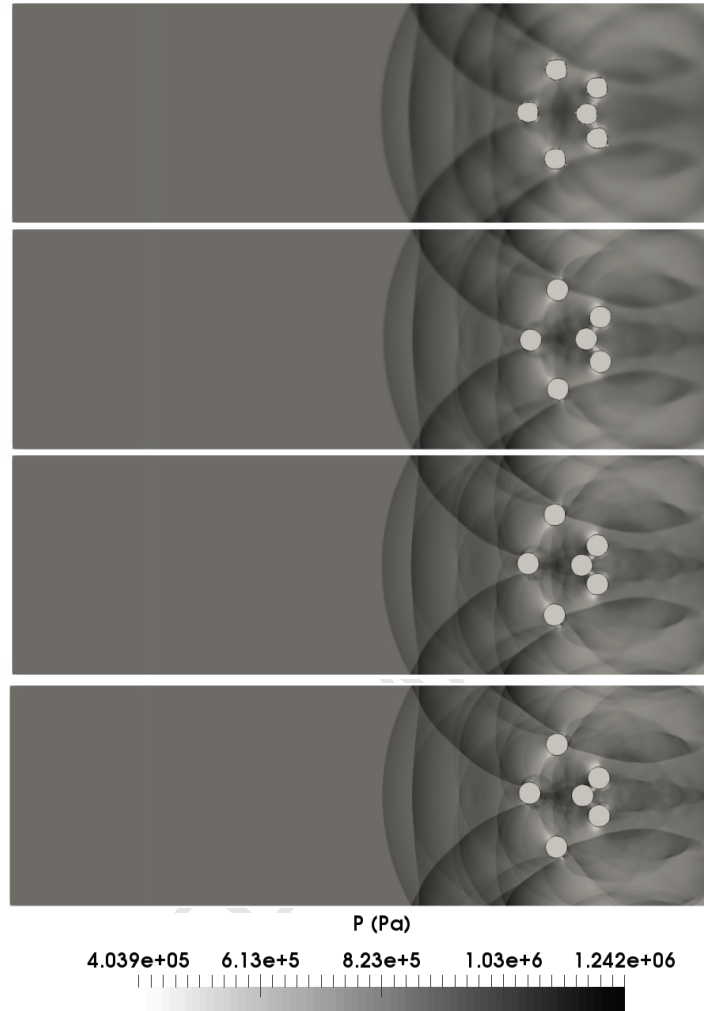


Figure 5.5- Mesh sensitivity analysis related to the computations of Fig. 5.4. Three meshes are considered: coarse with 40 222 cells, intermediate with 158 680 cells, fine with 616 454 cells and a very fine with 2 424 922 cells. The results are shown at time 0.336ms. The same qualitative evolution for the particle's dynamics is observed, in the direction of cluster formation.

Qualitative evolution regarding wave's dynamics as well as particle's motion is observed for any mesh resolution. Computed results on the last three meshes are very close, showing mesh independent behavior to form particle's cluster, at least in the present flow configuration and related initial data.

6. Conclusion

A Level-Set type method has been developed to track rigid bodies on unstructured meshes. Thanks to the Overbee limiter of Chiapolino et al. (2017) the method doesn't need reinitialization, nor interface reconstruction. A solid fluid coupling method has been built and compared to other approaches, based on stiff relaxation and conventional Ghost-Cell extrapolation. It is simple to implement and improves convergence. It has been extended to 2D and validated against 2D computations of supersonic flow around cylindrical body at rest. The overall method has been extended to two-way coupling and illustrations have been shown.

Acknowledgements. Part of this work has been supported by Excellence Initiative of Aix-Marseille University - A*MIDEX, a French "Investissements d'Avenir" programme, in the framework of the Labex MEC, as well as project SUBSUPERJET ANR-14-CE22-0014.

References

- Abgrall, R., Beaugendre, H., & Dobrzynski, C. (2014). An immersed boundary method using unstructured anisotropic mesh adaptation combined with level-sets and penalization techniques. *Journal of Computational Physics*, 257, 83-101.
- Barral, N., & Alauzet, F. (2018) Three-dimensional CFD simulations with large displacement of the geometries using a connectivity-change moving mesh approach. *Engineering with Computers*, 1-26
- Barth, T., & Jespersen, D. (1989) The design and application of upwind schemes on unstructured meshes. In *27th Aerospace sciences meeting* (p. 366)
- Baum, J., Luo, H., & Loehner, R. (1994). A new ALE adaptive unstructured methodology for the simulation of moving bodies. In *32nd Aerospace Sciences Meeting and Exhibit* (p. 414)
- Berger, M. J., & Colella, P. (1989) Local adaptive mesh refinement for shock hydrodynamics. *Journal of computational Physics*, 82(1), 64-84
- Chiapolino A., Boivin P., & Saurel R. (2017) A simple and fast phase transition relaxation solver for compressible multicomponent two-phase flows, *Computers and Fluids*, 150, 31-45
- Chiapolino A., Boivin P., & Saurel R. (2017) A simple phase transition relaxation solver for liquid–vapor flows, *International Journal for Numerical Methods in Fluids*, 83(7), 583-605
- Chiapolino A, Saurel R. Extended Noble–Abel Stiffened-Gas Equation of State for Sub-and-Supercritical Liquid-Gas Systems Far from the Critical Point. *Fluids*. 2018; 3(3):48
- Chiapolino, A., Saurel, R., Nkonga, B. (2017) Sharpening diffuse interfaces with compressible fluids on unstructured meshes. *Journal of Computational Physics*, 340, 389-417
- Chinnayya, A., Daniel, E., & Saurel, R. (2004) Modelling detonation waves in heterogeneous energetic materials. *Journal of Computational Physics*, 196(2), 490-538
- Farhat, C., Rallu, A., & Shankaran, S. (2008) A higher-order generalized ghost fluid method for the poor for the three-dimensional two-phase flow computation of under waterimplosions. *Journal of Computational Physics*, 227(16), 7674-7700
- Farhat, C., Gerbeau, J. F., & Rallu, A. (2012) FIVER: A finite volume method based on exact two phase Riemann problems and sparse grids for multi-material flows with large density jumps. *Journal of Computational Physics*, 231(19), 6360-6379
- Farhat, C., Lesoinne, M., LeTallec, P., Pierson, K., & Rixen, D. (2001) FETI-DP: a dual–primal unified FETI method—part I: A faster alternative to the two-level FETI method. *International Journal for Numerical Methods in Engineering*, 50(7), 1523-1544
- Fedkiw, R. P., Aslam, T., Merriman, B., Osher, S. (1999) A non-oscillatory Eulerian approach to interfaces in multimaterial flows (the Ghost Fluid Method). *Journal of Computational Physics*, 152(2), 457-492
- Glimm J, Grove J, Li X, Shyue K, Zeng Y, Zhang Q. (1998) Three-dimensional front tracking. *SIAM Journal of Scientific Computing*, 19:703–27
- Le Martelot, S., Saurel, R., & Nkonga, B. (2014) Towards the direct numerical simulation of nucleate boiling flows. *International Journal of Multiphase Flow*, 66, 62-78
- Le Métayer, O., Massoni, J., & Saurel, R. (2004) Élaboration des lois d'état d'un liquide et de sa vapeur pour les modèles d'écoulements diphasiques. *International journal of thermal sciences*, 43(3), 265-276
- Le Métayer, O., and Saurel, R. (2016) The Noble–Abel stiffened-gas equation of state. *Physics of Fluids*, 28(4), 046102
- Liu, T. G., Khoo, B. C., & Yeo, K. S. (2003) Ghost fluid method for strong shock impacting on material interface. *Journal of Computational Physics*, 190(2), 651-681
- Liu, T. G., Khoo, B. C., & Xie, W. F. (2006) The modified ghost fluid method as applied to

- extreme fluid-structure interaction in the presence of cavitation. *Communications in Computational Physics*, 1(5), 898-919
- Liu, T. G., Ho, J. Y., Khoo, B. C., & Chowdhury, A. W. (2008) Numerical simulation of fluid structure interaction using modified ghost fluid method and Naviers equations. *Journal of Scientific Computing*, 36(1), 45-68
- Muralidharan, B., & Menon, S. (2018) Simulation of moving boundaries interacting with compressible reacting flows using a second-order adaptive Cartesian cut-cell method. *Journal of Computational Physics*, 357, 230-262
- Nkonga, B., & Guillard, H. (1994) Godunov type method on non-structured meshes for three-dimensional moving boundary problems. *Computer methods in applied mechanics and engineering*, 113(1-2), 183-204
- Nkonga, B. (2000) On the conservative and accurate CFD approximations for moving meshes and moving boundaries. *Computer methods in applied mechanics and engineering*, 190(13-14), 1801-1825
- Olsson E, Kreiss G, Zahedi S. (2007) A conservative level set method for two phase flow II. *Journal of Computational Physics*. 225:785–807
- Saurel, R., Boivin, P., & Le Métayer, O. (2016) A general formulation for cavitating, boiling and evaporating flows. *Computers & Fluids*, 128, 53-64
- Saurel, R., & Pantano, C. (2018). Diffuse-Interface Capturing Methods for Compressible Two-Phase Flows. *Annual Review of Fluid Mechanics*, 50(1)
- Shewchuk, J. R. (2002) Delaunay refinement algorithms for triangular mesh generation. *Computational Geometry*, 22(1-3), 21-74
- Shukla RK, Pantano C, Freund JB. (2010) An interface capturing method for the simulation of multi-phase compressible flows. *J. Comput. Phys.* 229:7411–39
- Sweby, P. K. (1984) High resolution schemes using flux limiters for hyperbolic conservation laws. *SIAM Journal on Numerical Analysis*, 21(5), 995-1011
- Toro, E. F., Spruce, M., & Speares, W. (1994) Restoration of the contact surface in the HLL-Riemann solver. *Shock waves*, 4(1), 25-34
- Van Leer, B. (1979) Towards the ultimate conservative difference scheme. V. A second-order sequel to Godunov's method. *Journal of Computational Physics*, 32(1), 101-136
- Wang, C. W., Liu, T. G., & Khoo, B. C. (2006) A real ghost fluid method for the simulation of multimediuum compressible flow. *SIAM Journal on Scientific Computing*, 28(1), 278-302
- Wang, K., Rallu, A., Gerbeau, J. F., & Farhat, C. (2011) Algorithms for interface treatment and load computation in embedded boundary methods for fluid and fluid–structure interaction problems. *International Journal for Numerical Methods in Fluids*, 67(9), 1175-1206
- Wood, A. B. (1930) *A Textbook of Sound*. G. Bell and Sons Ltd., London
- Youngs, D. L. (1984) An interface tracking method for a 3D Eulerian hydrodynamics code. *Atomic Weapons Research Establishment (AWRE) Technical Report*, (44/92), 35
- Zalesak, S. T. (1979) Fully multidimensional flux-corrected transport algorithms for fluids. *Journal of Computational Physics*, 31(3), 335-362
- Zeng, X., & Farhat, C. (2012) A systematic approach for constructing higher-order immersed boundary and ghost fluid methods for fluid–structure interaction problems. *Journal of Computational Physics*, 231(7), 2892-2923